NERSC Technical Report no. 420

PHYSICAL OCEANOGRAPHY OF THE FRAM STRAIT

IMPROVING GENERAL UNDERSTANDING AND MODELS THROUGH THE USE OF MOORING INTERPOLATION PRODUCTS

by

François Challet
Florian Geyer
Laurent Bertino
Roshin P. Raj

Bergen, October 6th 2022

Nansen Environmental and Remote Sensing Center

Jahnebakken 3

N-5007 Bergen - NORWAY

Phone: +47 55 20 58 00

E-mail: admin@nersc.no

Web.site: http://www.nersc.no

a non-profit environmental research center
affiliated with the university of Bergen

REPORT

TITLE	REPORT No.
Oceanography of the Fram Strait – Improving general understanding and models through the use of mooring interpolation products	Technical report no. 420
CLIENT	**CONTRACT**
-	-
CONTACT PERSON (from Client)	**AVAILABILITY**
-	OPEN
AUTHORS / EDITORS	**DATE**
François Challet, Florian Geyer, Laurent Bertino, Roshin P. Raj	06/10/2022

SUMMARY

This report first develops an interpolation method for the Fram Strait mooring data. The resulting temperature sections are then compared with the acoustic data obtained during the ACOBAR experiment and are also used to assess the reliability of TOPAZ-4b in the Fram Strait. The last chapter links the temperature variability and trends observed in the Fram Strait with the circulation changes in the Nordic Seas and the Barents Sea and proposes an analysis of the underlying physical mechanisms.

APPROVAL

Project Leader: Laurent Bertino

Director: Tore Furevik

Table of Contents
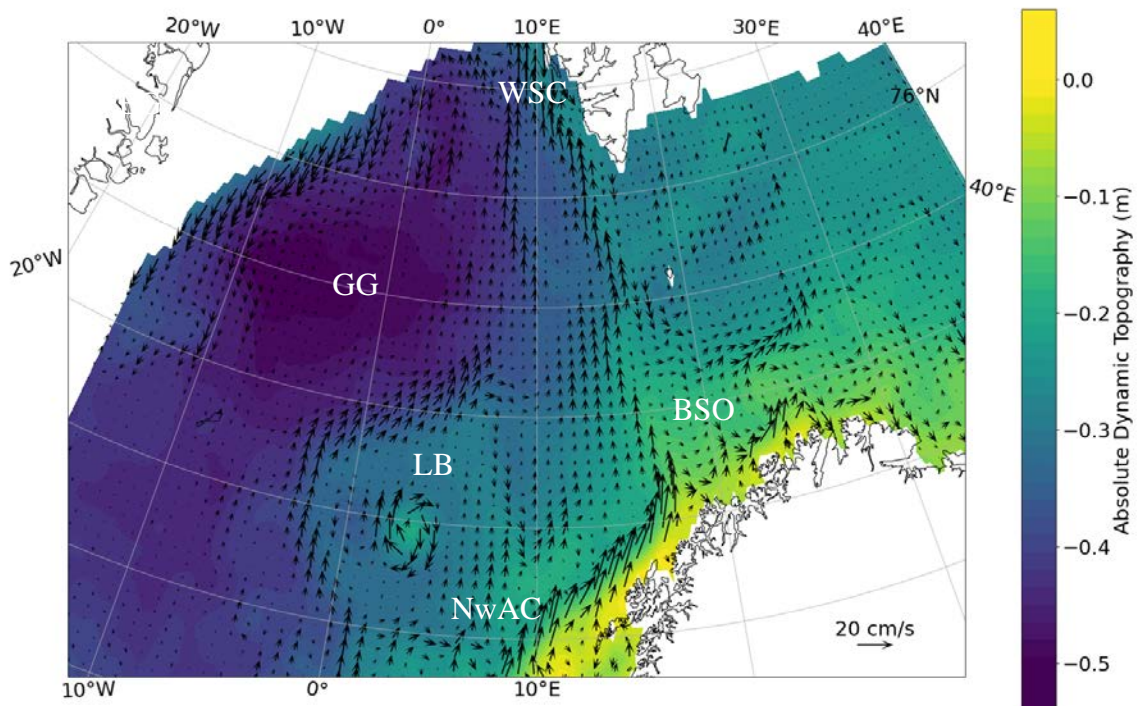
Introduction

The region spanning from the Nordic Seas to the Barents Sea connects the Arctic Ocean to the rest of the globe through two main gateways: the Fram Strait, which is the only deep water connection to the Arctic Mediterranean, and the Barents Sea Opening between Bear Island and the south of Svalbard. The Arctic Ocean is warming at more than twice the rate of the rest of the globe under the influence of climate change [1] and the warming reaches its maximum in the northern Barents Sea where fast sea ice retreat [2] has been associated with a transition of water masses properties known as Atlantification [25]. Understanding the impact of these changes on the oceanic circulation is crucial to predict future changes in heat transports to the Arctic.

Figure 1: Mean Sea surface temperature over the Nordic Seas and mean geostrophic currents calculated from the mean Absolute Dynamic Topography. WSC: West Spitsbergen Current, EGC: East Greenland Current, GG: Greenland Gyre, BSO: Barents Sea Opening, LB: Lofoten Basin, NwAC: Norwegian Atlantic Current

Figure 1 shows the main currents and oceanic basins which will be studied or mentioned throughout this report. The Norwegian Atlantic Current (NwAC) brings relatively warm and saline waters from the Atlantic to northern Norway. There, these waters split: part of them continues east to the Barents Sea through the Barents Sea Opening (BSO) while the rest continues north following the oceanic shelf and becomes the West Spitsbergen Current (WSC) [3]. The WSC is in fact divided in two branches coming from both branches surrounding the Lofoten Basin (LB): the WSC core along the coast of Svalbard and an offshore branch further west. A westward flow south of Svalbard also brings colder waters from the northern Barents Sea to the WSC. These warm Atlantic waters from the WSC eventually enter the Arctic Mediterranean or recirculate to the west in the Fram Strait at different latitudes [4]. West of the Fram Strait, finally, cold and fresh waters from the Arctic flow southwards via the East Greenland Current (EGC).

The understanding of the role of the Nordic Seas in the global climate has improved since the 1970s with an increasing number of oceanographic campaigns organized during the summer.

The region was discovered to be key to the Atlantic Meridional Overturning Circulation (AMOC) thanks to its role in deep waters formation. In the Greenland Sea and in the Barents Sea in particular, the interactions between relatively saline waters coming from the globe's oceans with a cold environment allows for the formation of dense waters likely to sink to the ocean bottom [5][6]. The links between changing water masses and sea ice cover are also of high importance in a context of global warming: increasingly warm and saline waters are flowing below the icecap but subduct below cold and fresh meltwater, making their influence on the ice melt uncertain [7].

The Fram Strait is a strategic point for all these interactions. Through the strait, which is barely 300km wide at 78.5°N, very different water masses are exchanged between the Nordic Seas and the Arctic Mediterranean, with warm and saline Atlantic waters flowing north along the coast of Svalbard, cold and fresh waters exported below the ice from the Arctic along the EGC and two main recirculation paths at 78.5N and 80°N [4]. But with variable forcings, such as winds, sea ice cover, and climate change, and high latitudes, the oceanic patterns are constantly changing. The Rossby radius typically ranges between 3 and 6 km in the WSC and the region is thus prone to the formation of eddies [4][8]. To understand this complex variability, a mooring line was deployed in the Fram Strait since 1997. Beszczynska-Möller et al. (2012) [9] published results from 1997-2010, which showed a significant warming trend of 0.06°C/year in the WSC, west of Svalbard. A strong positive temperature anomaly was also identified in 2006-07.

However, as estimations of the volume and heat exchanges are difficult to achieve with point measurements due to the small Rossby radius, integral measurements are also needed. An ocean acoustic tomography system consisting of three moorings with low frequency, broadband sources, and receivers was installed in the Fram Strait during 2010–2012 as part of the Acoustic Technology for Observing the Interior of the Arctic Ocean (ACOBAR) project [10]. They provide range-depth averaged time series of the water temperature in the region and offer a complementary vision over the temperature variability over two years [11].

The possibilities offered by the combined use of these two datasets will be studied throughout this report. The first step will be to interpolate the mooring data to create a usable tool for our analysis. The temperature interpolation will be done in two kriging steps, first reconstructing the anomalies from the seasonal cycle when data is missing and then estimating temperature values on each point of a regular grid. A detailed description of the interpolation method and of the resulting products will be given in the first chapter. In the second chapter of this report, the interpolated data will be compared with the acoustic datasets to check their consistency, but also better understand the geographical temperature correlations over the region covered by the data. A frequency analysis of these correlations will be performed to estimate the time scales for which they are valid. Both datasets will then be used to quality-check a coupled ocean-sea ice model developed by NERSC (Nansen Environmental and Remote Sensing Center), TOPAZ-4b [12][13], in the third chapter.

Finally, the fourth and last chapter of this report will focus on the understanding of the physical processes responsible for the observed interannual and long-term variability, both in the Fram Strait and on a wider scale. Several studies have proposed mechanisms to explain the temperature anomalies in the Fram Strait. One of the explanations relies on a strengthening of the Greenland Gyre driven by low-pressure anomalies which would intensify the northward current to the Fram Strait (Chatterjee et al., 2018 [14]). The decrease in sea ice export through the western Fram Strait was also identified to increase salinity in the Greenland Sea, which could also eventually increase the gyre circulation (Wang et al., 2020 [15]). Altimetry datasets from CMEMS and ERA5 reanalyzes will here be used to test some of these mechanisms and push further our understanding of the variability and trends in the Fram Strait, the Nordic Seas and the Barents Sea.

I.   Description of the mooring data and of the interpolation process

This chapter will describe the method used to obtain interpolated products for the mooring data in the Fram Strait. We will first briefly describe the content of the raw dataset and highlight the main challenges faced during the interpolation process. Then, the different steps of the method will be presented using the temperature data. The adaptation of the method to salinity and velocity data will finally be addressed.

1) Description of the mooring data

Our analysis of the oceanography of the Fram Strait is based on the data collected along the mooring line deployed at 78.5°N between August 1997 and August 2016 [9] *(Beszczynska-Möller, 2012)*. The range of longitudes covered by the mooring array spans between 6.5°W and 8.7°E, including all the deep part of the strait. Its precise location is shown on Figure 2. The coast of Greenland is located beyond 15°W, but all the region between 6.5°W and 15°W has a relatively shallow bathymetry which limits the volume transport through these longitudes. The twelve moorings located in the eastern and central Fram Strait were maintained by the Alfred Wegener Institute while the westernmost four moorings were operated by the Norwegian Polar Institute.
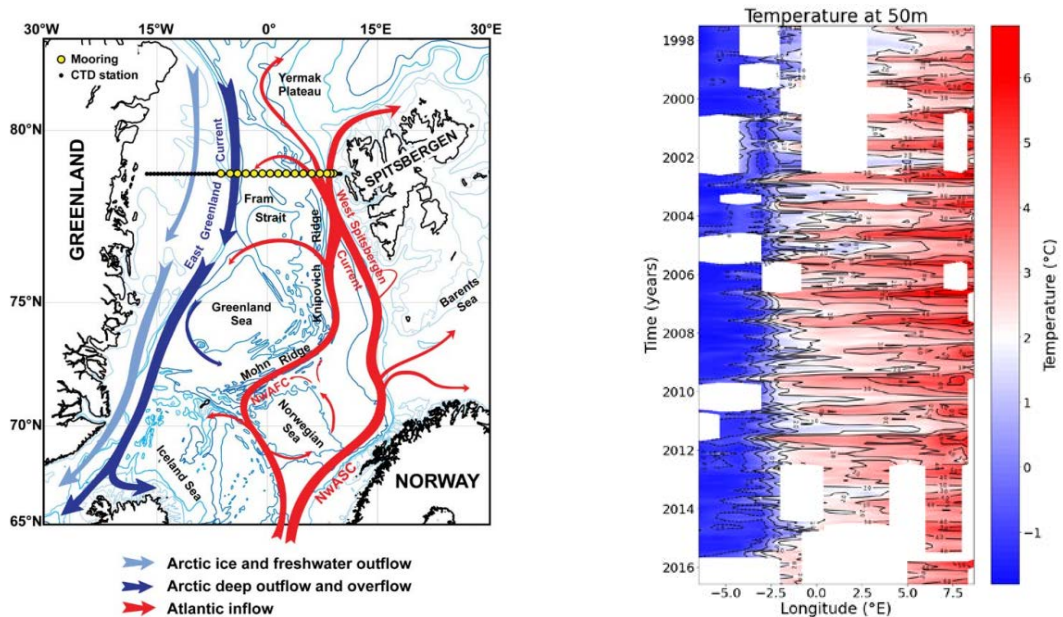
Figure 2 – left: Main current and bathymetric features in the Nordic Seas and location of the mooring array (figure taken from [9]) – right: Hovmöller diagram for the temperature at 50m – white areas correspond to the gaps in the data

All moorings are instrumented at standard levels: subsurface (50m), Atlantic Water (AW) layer (250m), AW layer lower boundary (750m), deep waters (1500m where available) and the near-bottom level (10m above the bottom). At 50m, 250m and at the ocean bottom, temperature and velocity sensors provide hourly data for most moorings. A large fraction of the moorings also provides measurements at 750m and 1500m but part of the data was missing for these two depths. Table 1 shows the total number of hourly temperature measurements obtained between 1997 and 2016 for the mooring located at 5°E.

Depth range	0 – 100m	100 – 400m	400 – 1000m	1000 – 1800m	1800m - bottom
Nb of measurements	200 676	170 892	81 853	64 540	160 897

Table 1: number of temperature measurements obtained at 5°E for each of the five instrument depths

Most moorings were also equipped with salinity sensors at 50m and 250m. A few salinity measurements were performed in deeper waters as well, but they were obtained with different sensors and were often faulty *(Beszczynska-Möller, personal communication)*.

The time series at each instrument location have a high resolution (hourly measurements) but may also contain gaps for some years, even in the subsurface where the measurements were more numerous. The Hovmöller diagram presented in Figure 2 shows the temperature at 50m as well as the locations and years where data was missing, represented with white rectangles.

In total, we calculate that temperature values are missing on average for 40% of the instrument locations. The regions with a lower data density will be responsible for the main challenges in the interpolation process described in this chapter.

2) The choice of the interpolation method: a crucial step for the understanding of the oceanography of the Fram Strait

One of the main motivations behind the deployment of the mooring array in the Fram Strait was to estimate the volume and heat transport between the world's oceans and the Arctic. Tsubouchi et al explained that the total volume transport to the Arctic, taking into account all entrances to the Arctic Mediterranean, could not be closed properly with the available data [16]. The Fram Strait was the main source of uncertainty, with a volume transport estimated as -2.0 Sv +- 2.7 Sv.

Our motivations for interpolating the data are twofold. One objective is the comparison of the mooring data with the results of the ACOBAR project, a tomography experiment carried out between 2010 and 2012, which measured range-depth-averaged temperatures along several paths [10][11]. The second one is the model evaluation of TOPAZ-4b, the latest version of the coupled ocean-sea ice model developed by NERSC.
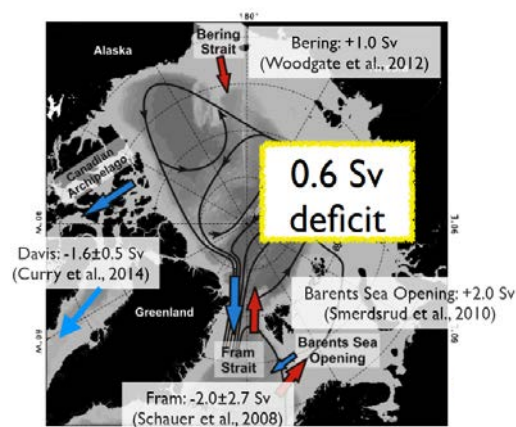

Figure 3: Volume transport in each gate to the Arctic Mediterranean, figure from Tsubouchi et al, 2017

The interpolation of the temperature and velocity values was first performed by *Beszczynska-Möller et al* [9] to calculate the volume transport and Atlantic Water (defined as water masses

above 2°C and 34.9 psu) transport by the West Spitsbergen Current. These interpolated products are however not available to the public. The authors proceeded in several steps: first filling the aforementioned gaps in the measurements and then using a kriging algorithm to obtain temperature values on a regular grid with a vertical resolution of 5m and a horizontal resolution of 1km (*Beszczynska-Möller et al, personal communication;* [9]).

Due to the large temperature variations over the section – between the WSC and the EGC, between subsurface and deep waters – and since the Rossby radius is smaller than the horizontal distance between two measurements, the interpolation is likely to have a considerable influence on depth-averaged temperatures in the strait. Several choices of interpolation methods are compared on Figure 4: two 1D methods computing temperature values as linear combinations of the measurements available over the water column (weights decrease with the inverse of the cube of the distance or exponentially); a 1D method using cubic-spline interpolation [17] and the result of the kriging algorithm which will be detailed later in this chapter.
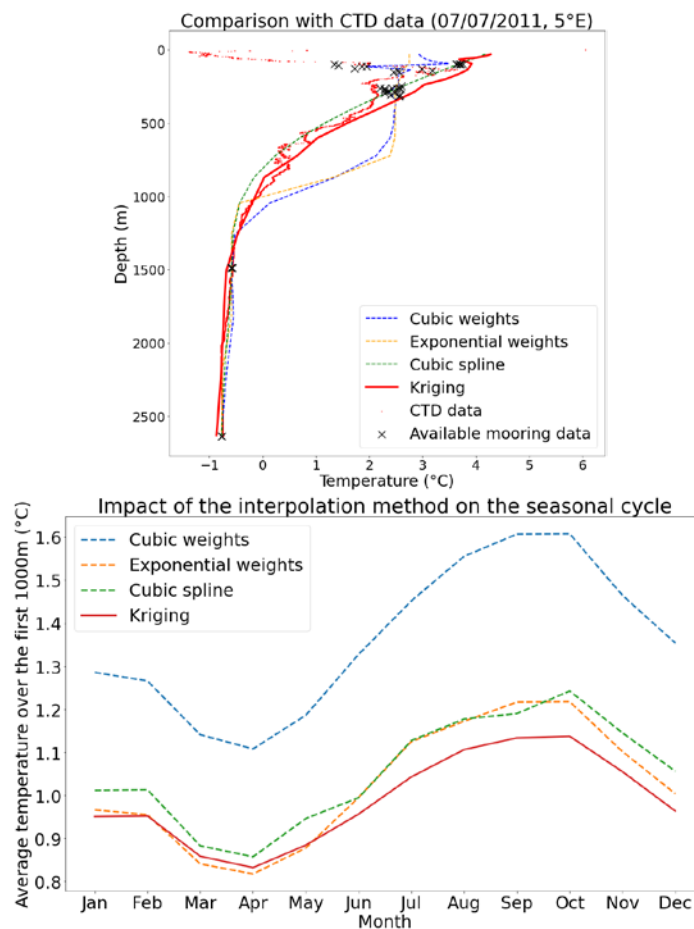
Figure 4: Impact of the interpolation method on the temperature profile – left: comparison of the temperature profiles obtained at 5°E on 07/07/2011 with different methods with CTD data – right: impact of the interpolation method and the range-depth-averaged seasonal cycle between 0m and 1000m and 4°W and 8°E

The comparison with CTD data highlights that, when the temperature varies a lot between two consecutive data points, interpolation methods are likely to generate large errors in between. In particular, on Figure 4, 1D methods using cubic or exponential weights largely overestimated the temperature between 500m and 1000m due to the absence of data at 750m. Such errors then generate large biases in depth-averaged temperatures. On Figure 4, the difference in the mean temperature obtained with different methods – up to 0.4°C - can exceed the total amplitude of

the seasonal cycle. The amplitude of the seasonal cycle is also affected by the choice of the interpolation method and can vary by 50%.

3) An interpolation method based on ordinary kriging

The interpolation is performed on a regular grid with a resolution of 0.5° along the horizontal axis and 31 depth layers along the vertical axis, with values every 5m close to the surface and a lower resolution in deeper waters. Two temperature products are obtained, with monthly and daily time steps. First, a 3D-kriging algorithm (time-depth-longitude) estimates the monthly temperature anomalies even when no measurement is available for a mooring location, and then a 2D-kriging algorithm provides temperature values for all points of any regular grid. Both these steps rely on ordinary kriging, whose general principle will be briefly described, before detailing its application to each of the interpolation steps.

Ordinary kriging [18] is probably the most common interpolation method for several dimensions. The principle is to estimate the value of a variable at a location (x_0 on Figure 5) using known values in neighbouring locations in space.

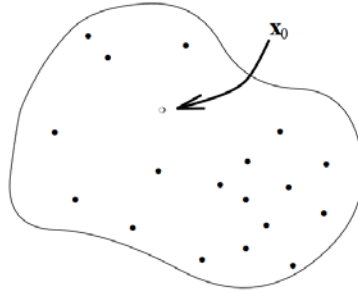*Figure 5: principle of ordinary kriging (taken from[18])*

Knowing a value for each location x_α, we are trying to define an estimator $Z_{OK}^*(x_0)$ with the following form [18]:

$$Z_{OK}^\star(\mathbf{x}_0) = \sum_{\alpha=1}^{n} w_\alpha Z(\mathbf{x}_\alpha)$$

where w_α are coefficients to be determined.

Such an estimator is unbiased. Assuming that the data are part of a realization of a random variable $Z(x)$, the estimation variance σ_E^2 is:

$$\begin{aligned}
\sigma_{\mathrm{E}}^2 &= \mathrm{E}[\,(Z^\star(\mathbf{x}_0) - Z(\mathbf{x}_0))^2\,] \\
&= -\gamma(\mathbf{x}_0-\mathbf{x}_0) - \sum_{\alpha=1}^{n}\sum_{\beta=1}^{n} w_\alpha\, w_\beta\, \gamma(\mathbf{x}_\alpha-\mathbf{x}_\beta) + 2\sum_{\alpha=1}^{n} w_\alpha \gamma(\mathbf{x}_\alpha-\mathbf{x}_0)
\end{aligned}$$

where the function γ is called a variogram. Its purpose is to describe how much the variable is susceptible to vary between two locations separated by a certain distance [18].

Introducing a Lagrangian multiplier μ_{OK}, we want to minimize the variance of the estimator under the constraint that the weights w_α should add up to 1. This gives us the system of equations for ordinary kriging [18] from which we can find the values of the weights w_α.

$$\begin{pmatrix} \gamma(\mathbf{x}_1-\mathbf{x}_1) & \cdots & \gamma(\mathbf{x}_1-\mathbf{x}_n) & 1 \\ \vdots & \ddots & \vdots & \vdots \\ \gamma(\mathbf{x}_n-\mathbf{x}_1) & \cdots & \gamma(\mathbf{x}_n-\mathbf{x}_n) & 1 \\ 1 & \cdots & 1 & 0 \end{pmatrix} \begin{pmatrix} w_1^{\mathrm{OK}} \\ \vdots \\ w_n^{\mathrm{OK}} \\ \mu_{\mathrm{OK}} \end{pmatrix} = \begin{pmatrix} \gamma(\mathbf{x}_1-\mathbf{x}_0) \\ \vdots \\ \gamma(\mathbf{x}_n-\mathbf{x}_0) \\ 1 \end{pmatrix}$$

Inverting this system should give the weights needed to calculate the interpolated value at location x_0. However, the variogram γ still needs to be defined, and it can only depend on the vector separating two points. The main difficulty is that, depending on the location within the Fram Strait, a same distance can imply huge temperature changes or almost none (up to 4°C between the surface and 500m deep and then very small variations down to the ocean bottom). This means kriging cannot be performed in the real space without inducing large errors between 250m and 750m.

Therefore, for both interpolation steps, we first define a new space in which a given vertical or horizontal translation always induces variations of a similar amplitude of the interpolated variable. A more accurate description of these spaces will be given in the sections detailing each of the two kriging steps.

4) <u>First kriging step: interpolation of the temperature anomalies</u>

Ahead of the first interpolation step, we discard all the values deviating from the local seasonal cycle by more than three standard deviations.

All time series at instrument locations (except for 2 located in the western Fram Strait) contain enough data to calculate the local temperature seasonal cycle with a monthly resolution. These climatologies provide a first estimate of temperature values in the gaps, but do not contain any information on interannual variability and anomalies.

The temperature anomalies are estimated using the available data at other time steps and instrument locations. It can be shown that the correlation between the normalized temperature anomalies at neighbouring instrument locations is in most cases higher than 0.4 both along the vertical and the horizontal axes. These correlations are significant above 750m where the autocorrelation is lost after a few days. The autocorrelation times are longer close to the ocean bottom where the signal is dominated by the trend of global warming. In either case, neighbouring data points in time or space can be used to infer a missing value at a mooring location.

Figure 6 illustrates the evolution of the autocorrelation at several depths at 1.6°E.
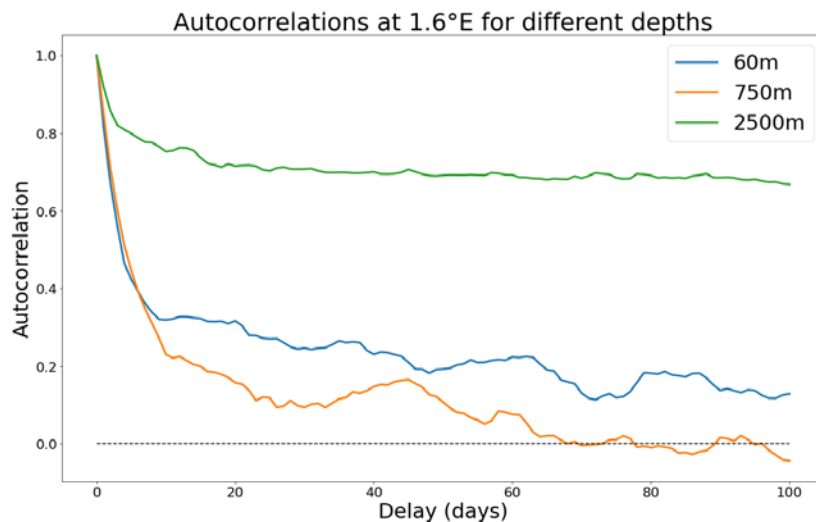

Figure 6: Autocorrelations at 60m, 750m and 2500m for the mooring located at 1.6°E

The temperature anomalies are estimated using a 3-dimension kriging algorithm, which calculates each anomaly as a linear combination of known anomalies at other locations or at another time step. To make the implementation of kriging possible, the data is considered in a new space, where the three dimensions are no more temporal and spatial but are redefined depending on temporal and spatial variations of temperature anomalies. More precisely, we calculate the average variations in temperature anomalies between consecutive months, neighbouring water columns and consecutive instrument depths. The results allow us to define the new space where all distances reflect the order of magnitude of temperature anomaly variations. In this new space – later referred to as the "kriging space" -, the variogram γ used for kriging is defined as:

$$\gamma(d) = 1 - e^{-d}$$

where d is the distance between two points. Such a variogram generates an effect of screening, which means that remote measurements should have very little impact on interpolation [18].
The implementation of the kriging equations then provides, for most mooring locations, a complete time series for the temperature anomaly between 1997 and 2016. The kriging theory also gives an estimate of the uncertainty on the result. However, this value does not take into account the effects of the projection of the data into the kriging space and the irregularities in spatial and temporal correlations (domination of temporal correlations in deep water and spatial correlation at the surface).
 The validity of the method is checked by removing some of the available measurements and recalculating the values with the kriging algorithm. We perform two tests by removing the values for 12 months in 2006 at 250m in the offshore branch of the WSC. Year 2006 was characterized by a strong warm anomaly which we want to replicate where data has been removed. The tests are defined as follows:

➢ Test 1: only the measurements at 250m for one mooring are removed. This is done to assess the ability of the algorithm to reconstruct the signal from neighbouring points.
➢ Test 2: the measurements at 250m for the two neighbouring moorings are also removed, as well as the measurements at 50m and at 750m at the test location. Therefore no close data point is available, which is done to replicate a situation similar to that of the larger gaps in the mooring data.

The results of the kriging algorithm applied to these two tests are presented on Figure 7.
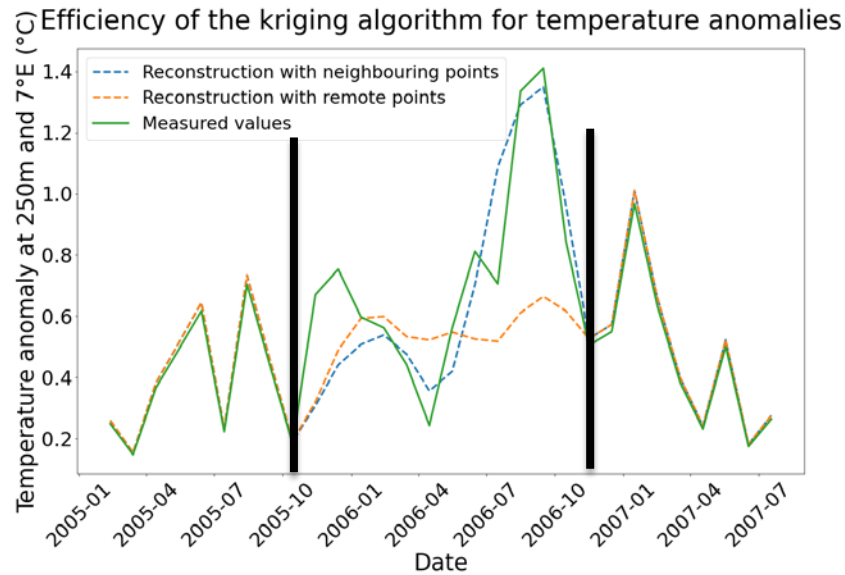
Figure 7: Test of the efficiency of the kriging algorithm to estimate missing temperature anomalies, the black vertical lines indicate where data has been removed

When values close to the removed data are available, the algorithm successfully replicates the temperature evolution with quite a good precision (error inferior to 0.3 °C). When neighbouring values are also removed, the precision of the pattern is significantly reduced but the order of magnitude of the temperature anomaly over the 12-month test period is still correct (+0.6°C). Even in this case, the kriging algorithm therefore improves on the estimation of the temperature anomaly.

Going further, we perform a larger number of such tests and estimate the error between the result of kriging and the observations. The results are summerized in the table below. The error is defined as the square of the difference between result and observations, summed over the 12 months of the test:

$$Error = \sum_{m=1}^{12} (T_{kriging} - T_{measured})^2$$

Depth	Number of tests	Average error when using the **uncorrected seasonal cycle** (°C²)	Average error when reconstructing the anomaly from the **neighbouring points** (°C²)	Error when reconstructing the anomaly from **remote points** (°C²)
60m	8	3.20	0.92	2.57
250m	8	2.86	1.12	1.71
2400m	7	0.014	0.004	0.004

Table 2: quality-check of the method to reconstruct temperature anomalies – the 23 tests performed for various dates and longitudes grouped by instrument depths

Even if the kriging of the anomalies does not improve the result in all individual tests compared to the uncorrected seasonal cycle, it reduces the average error for all tested depths, even when the anomalies are extrapolated from remote moorings. Besides, we also note that the distance between the available data and the reconstructed point has a larger impact closer to the surface, where the spatial correlation is stronger than the temporal autocorrelation between consecutive

months. On the contrary, temporal autocorrelation has a stronger impact in deep waters where both tests manage to divide the error by 3 compared to the uncorrected seasonal cycle.

Therefore, this first kriging algorithm successfully fills the gaps in the measurement time series at all instrument locations. The method proves to provide considerably better estimates of the temperature values than those given by local seasonal cycles.

5) Inclusion of Sea Surface Temperature (SST) data

The comparison on Figure 8 between subsurface waters at 50m and with the monthly satellite SST measurements available on Copernicus Marine Service (CMEMS) shows that the temperature can vary by several degrees in the first meters below the surface. In particular in the central Fram Strait, surface temperatures can be 2°C to 3°C colder than the water temperature at the first mooring depth. This strong surface cooling is linked to the frequent presence of sea ice in the central Fram Strait: melting patches of drifting ice provide a cold and fresh water input at the surface with a lower density than the warmer waters recirculating below from the WSC.
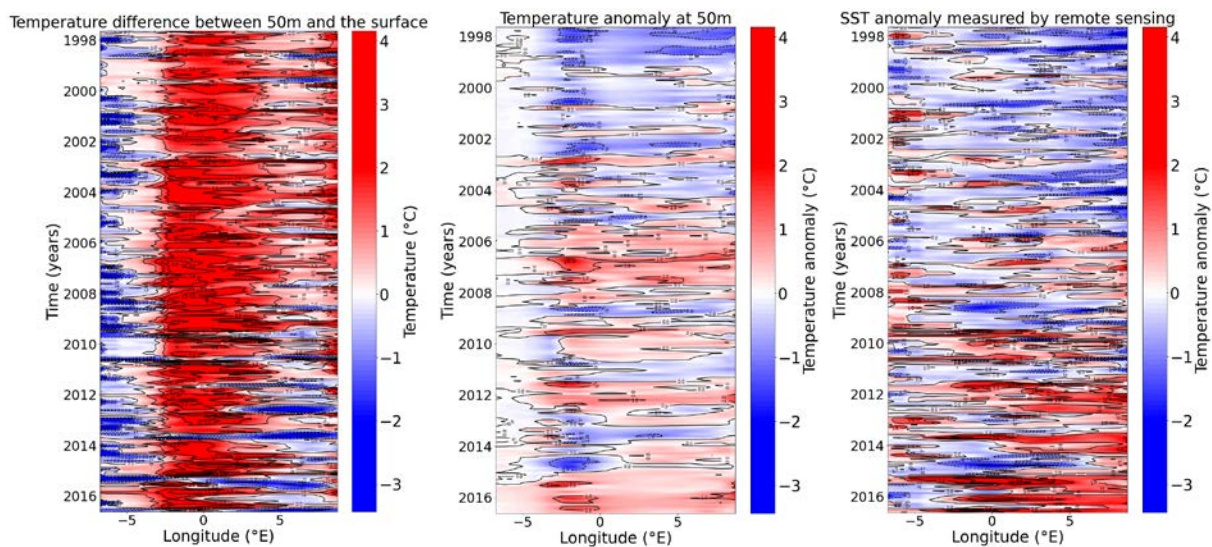

Figure 8: Comparison of the surface and subsurface temperatures over the period 1997-2016 – Left: difference between the temperature at 50m and the measured SST – Center: Temperature anomalies at 50m – Right: SST anomalies.

Also, the previous figures highlight that the main patterns of the interannual variability differ between the surface (right) and the subsurface (center). Though the 2006-07 warm anomaly is visible on both diagrams, it is much more obvious in subsurface waters. On the contrary, surface variability is mostly dominated by effects of global warming as most warm anomalies occurred after 2011.

To capture the different mechanisms affecting surface and subsurface waters in the interpolated datasets, another layer of data is added at the surface using the SST measurements presented on Figure 8. The final interpolation of the monthly temperatures described in the next section is thus performed from 6 layers of data and 16 mooring locations.

6) Second kriging step: obtention of monthly and daily interpolated temperature products

This final interpolation step is done using another kriging algorithm. The interpolation is performed for each month or day separately – this kriging algorithm is thus implemented in a 2D space, while the first kriging step was done in a 3D space. Once more, the data is moved

from the real space to a new space, defined from the average temperature (instead of the temperature anomalies used for the first step) variations between neighbouring instrument locations. The conversion of the vertical distances is illustrated on Figure 9.
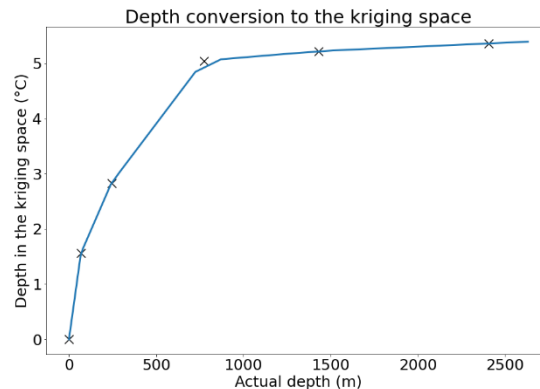

Figure 9: Conversion of mooring depths to the kriging space. Black crosses represent the average mooring depths.

In this new space, the variogram γ is once more defined as:

$$\gamma(\mathrm{d}) = 1 - e^{-d}$$

where d is the distance between two points.

To reduce the size of the matrices to invert, only the data horizontally closer than 3°C and vertically closer than 2°C in the new space is used in the calculation of each interpolated value. The result of this final interpolation step is presented on Figure 10. The average temperature section displays the main oceanic features expected in the region, with a warm WSC to the east, a cold EGC to the west and relatively warm waters recirculating in the central Fram Strait.
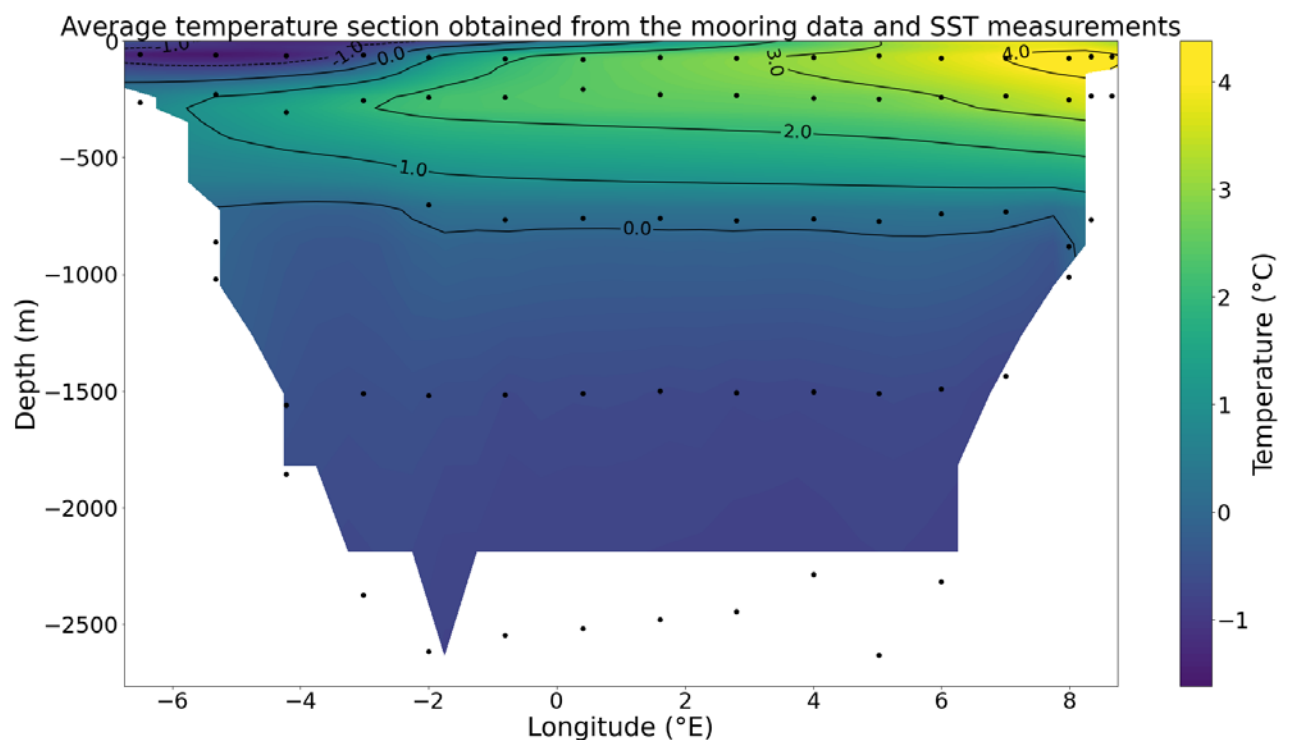

Figure 10: Average temperature section obtained with ordinary kriging

The obtention of the monthly and daily interpolated products stems from the same algorithm. However, the correlations which were used to fill the gaps in the data were the result of low-frequency anomalies with typical time scales of a few months. These correlations are lost along the horizontal axis at higher-frequencies as most of the variability then results from small-scale eddies. Therefore, only the low-frequency part of the signal (time scale longer than a month) can be reconstructed in the daily interpolated product.

Besides, the satellite SST dataset used to complement the mooring data only had a monthly resolution. Therefore, no SST data is included in the daily interpolated product, which thus stops in subsurface waters at a depth of 30m, and only includes 25 vertical levels.

The quality of the interpolated products is evaluated against independent CTD data. Two examples are presented on Figure 11 but qualitative comparisons for other locations were performed, showing similar results.
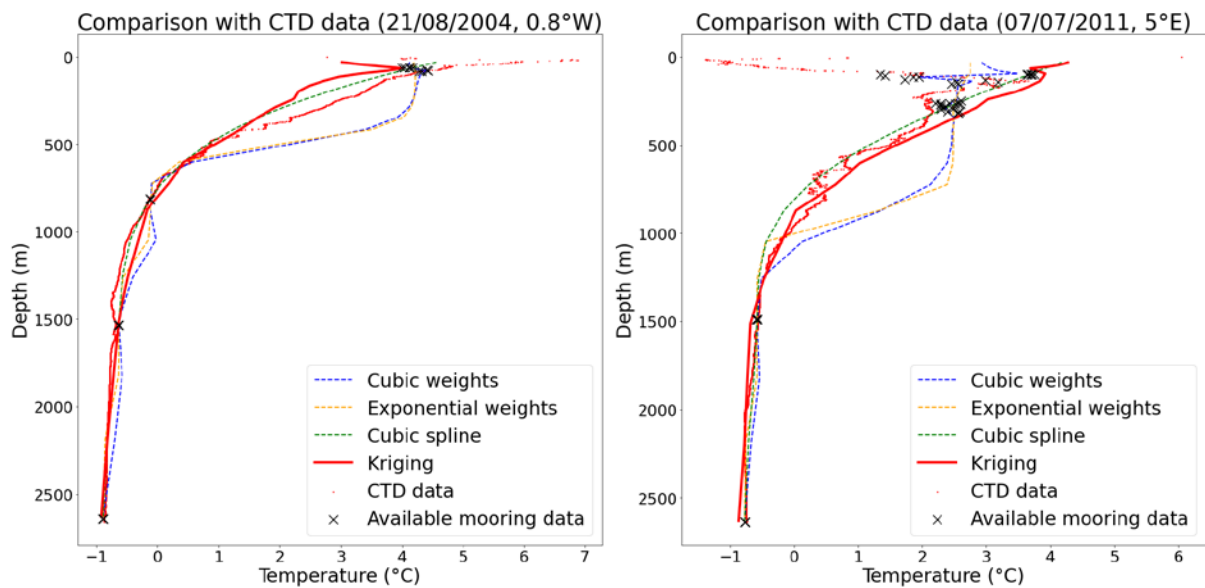

Figure 11: Comparison of the different interpolation methods with CTD profiles - left: at 2°W on 21/08/2004 – right: at 5°E on 07/07/2011

The comparison is done using the daily product and shows that no significant systematic bias is induced between consecutive instrument depths: kriging always gives a result at least as good as the best of the simpler vertical interpolation methods mentioned in section 2). This qualitative result validates the algorithm used for the second kriging step, which is the same for the daily and monthly products.

Both kriging algorithms provide an estimate of the uncertainty of the results and, though no rigorous way of combining the two could be found, adding the variances related to both kriging steps provides a maximum estimate for the uncertainty of the monthly interpolation. The uncertainty on the daily interpolation also takes into account the fact that the high-frequencies cannot be estimated when some measurements are missing; the resulting uncertainty contribution for each location is calculated from the difference between daily temperatures and monthly averages. Figure 12 shows the average total uncertainty on the final temperature for the monthly product. The highest values are obtained between 250m and 750m, where the temperature variation between two measurements is the largest. The uncertainty is always smaller than 1°C and generally below 0.6°C which is much smaller than the scale of the temperature variations of up to 6°C observed within the section.
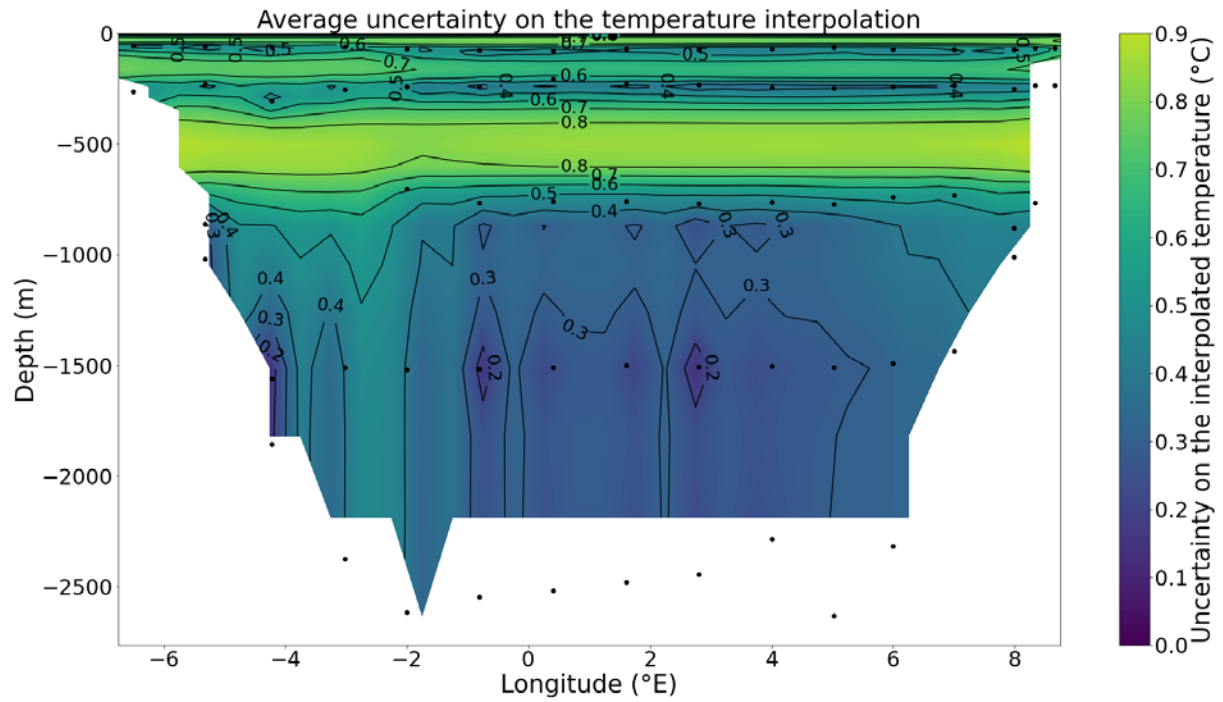
Figure 12: Average uncertainty on the interpolation result after the two kriging steps

7) <u>Adaptation of the interpolation algorithm to salinity and current velocity data</u>
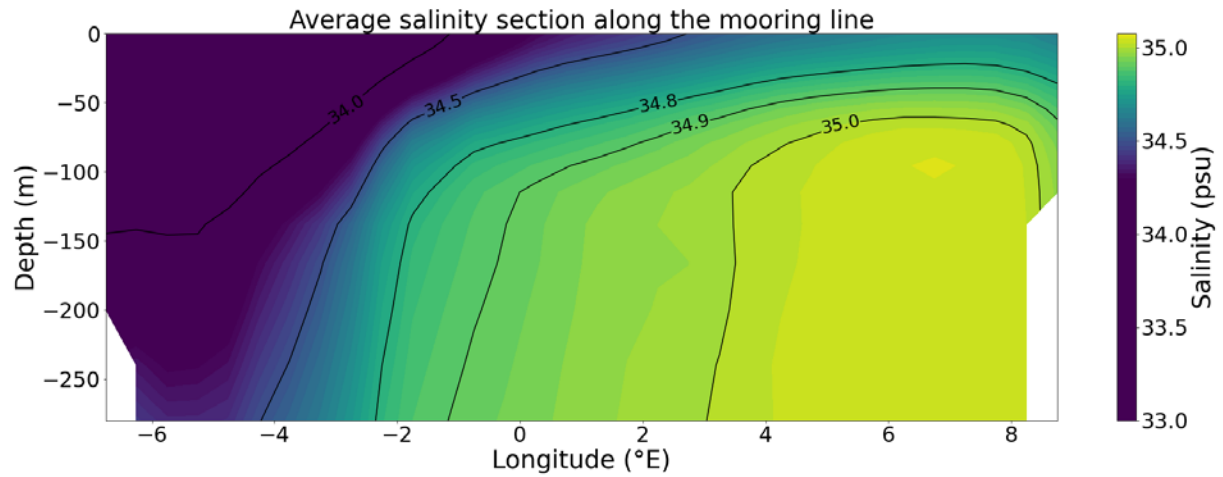

Figure 13: Average salinity section over the first 280m – the interpolation was done using both the mooring data up to 250m and surface salinity measurements by remote sensing
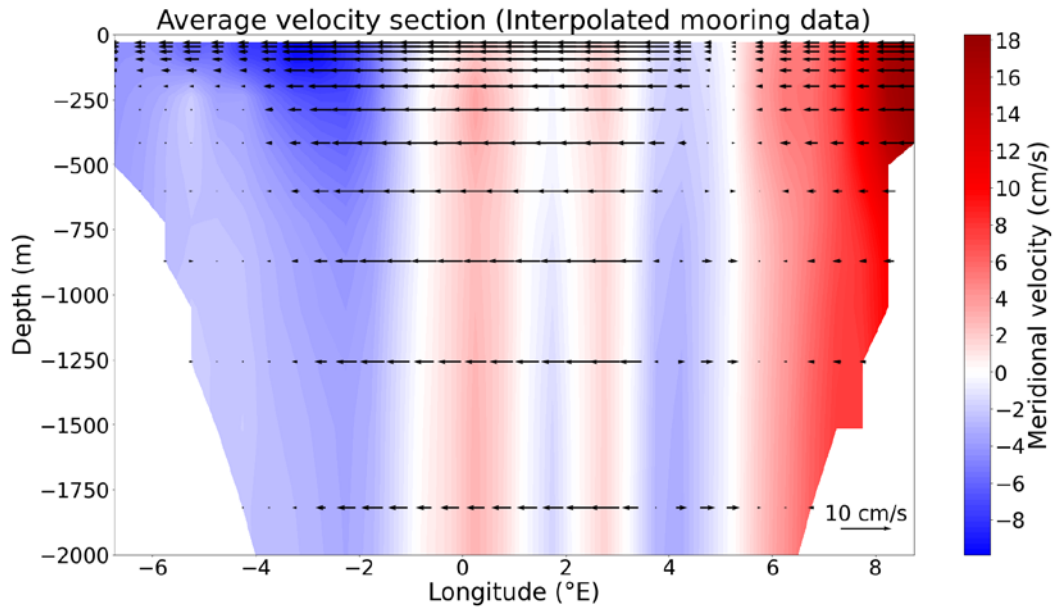
Figure 14: Average current velocities – the colors represent the meridional currents and the arrows the zonal currents

Since the moorings in the Fram Strait also provide salinity and velocity measurements, these quantities are also interpolated with monthly time steps, but with the following limitations:

➢ The salinity values measured below 250m were either missing or unreliable *(Beszczynska-Möller, personal communication).* The interpolated product is thus only obtained over the first 280m, using data from the first two instrument depths complemented by surface salinity measurements by remote sensing.

➢ The current velocities can vary a lot over small time scales and small eddies can always be found along the mooring line. Therefore, the horizontal correlation between neighbouring moorings is close to 0 and the auto-correlations in the data are also very weak. For this reason, the reconstruction of the anomalies where data is missing cannot be done using the same algorithm as for the temperature and the salinity. Missing data is simply replaced by values from the seasonal cycle, which is far from ideal. It nevertheless guarantees that no artificial anomaly is generated by the interpolation.

These two interpolated datasets can still provide useful information on the general salinity and velocity patterns in the Fram Strait. The salinity maximum in the WSC is found below 100m and reaches 35.1 psu, while surface waters are fresher (around 34.7 psu). Though the strongest currents are located in the first 500m, both the meridional and recirculation currents show a quite barotropic structure. We also note the existence of a velocity minimum around 5°E between the WSC and the recirculation branch. These results are consistent with those presented by Beszczynska-Möller in [9].

These interpolated datasets will be valuable for comparisons with the range-depth averaged temperature measurements derived from the ACOBAR acoustic experiment and the model evaluation of the ocean model TOPAZ-4b. These applications will be detailed in the following two chapters.

II. Comparison between mooring and acoustic data

1) <u>Motivation: two complementary datasets</u>

Between September 2010 and summer 2012, acoustic sources and receivers were deployed in the Fram Strait in the frame of the ACOBAR project (Acoustic Technology for Observing the interior of the Arctic Ocean) [10][11]. By measuring the sound speed along several acoustic paths, integrated temperature values were obtained along these paths through inversion. Such temperatures are averages over the first 1000m of the ocean and the whole path between the source and the receiver. Figure 15 shows the locations of the different acoustic instruments.
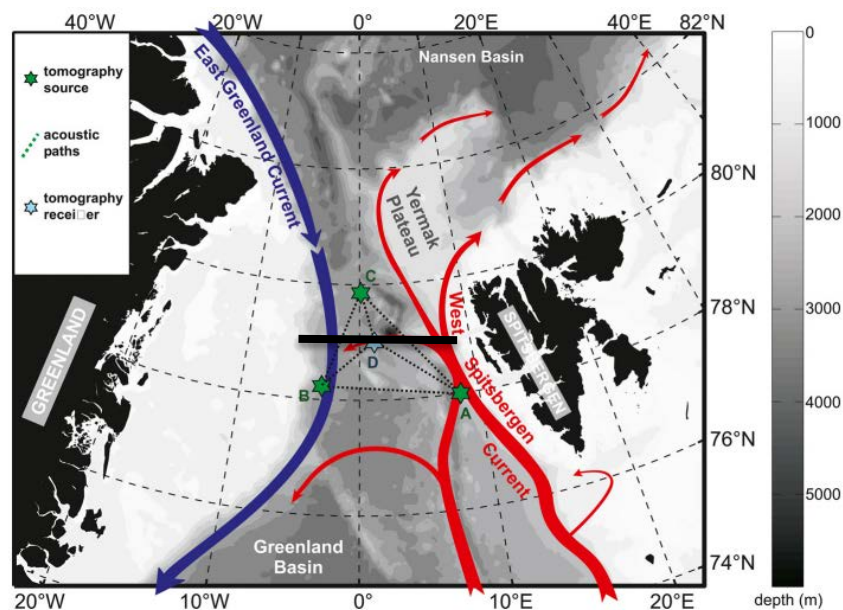

Figure 15: Locations of the acoustic instruments used in the ACOBAR experiment (from [11]) – The mooring C was lost at the start of the experiment – The horizontal black line indicates the location of the mooring section whose data was interpolated in the first chapter.

Acoustic data was obtained for paths A-B, B-A, A-D and B-D. The receiver D is located at the middle of the mooring line. Such data can provide complementary information to the interpolated mooring data for several reasons:

➢ The result is a depth average which can be used to check the consistency of the interpolation result in a different way.
➢ Points A and B are located further south in the Fram Strait and can broaden our geographic vision of the oceanographic processes in the Fram Strait.
➢ Small-scale eddies located between two mooring instruments may not be captured by the interpolation. Acoustic data could provide information on high-frequency events occurring on the paths.

2) <u>Consistency between the two datasets</u>

Before combining the information provided by the two datasets, we check their consistency with each other. One possibility is to compare the seasonal cycles obtained from the different acoustic paths to the result of the mooring data interpolation between 4°W and 8°E, where the bathymetry exceeds 1000m.
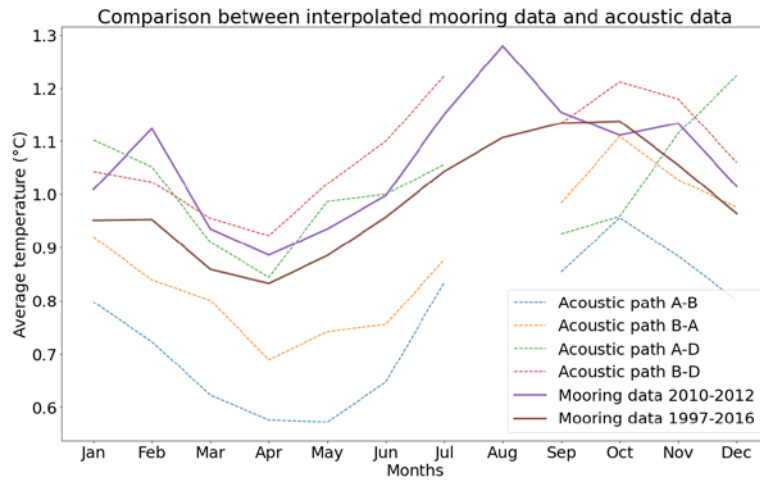
Figure 16: Seasonal cycle comparison between acoustic data and interpolated mooring data

Dataset	Range-depth averaged temperature	Total amplitude
Acoustic path A – B	0.75°C	0.38°C
Acoustic path B – A	0.88°C	0.42°C
Acoustic path A – D	1.02°C	0.38°C
Acoustic path B - D	1.08°C	0.30°C
Interpolated mooring data 2010 – 2012	1.06°C	0.39°C
Interpolated mooring data 1997 - 2016	0.99°C	0.31°C

Table 3: Compared range-depth averaged temperatures over the first 1000m and seasonal cycle amplitudes

The seasonal cycle is calculated from the mooring data both over the period 2010-2012 (ACOBAR project) and over the whole 1997-2016 period. Both results compare well with most of the acoustic paths when considering the average temperature and the amplitude of the seasonal cycle. Yet, it can be observed that paths A-B and B-A are slightly colder than the other acoustic paths and the mooring line located further north. This could be due to warmer Atlantic Waters recirculating further north, along paths A-D and B-D and the mooring line. Hattermann et al. showed that most of the recirculations – either driven by the Greenland Gyre or by eddies – were taking place at 78.5°N and 80°N [4]; this should mean that the fraction of warm Atlantic water is higher at such latitudes than along the path A-B. We finally note the more irregular pattern obtained for path A-D, with a surprising temperature maximum in December.

3) Spatial correlations between acoustic and mooring data: which water masses circulate along the acoustic paths?

Since all acoustic paths are located south of the mooring section, further comparisons between the two datasets can be done to study the geographical extent of temperature anomalies in the Fram Strait. If a warm anomaly is observed south-east of the mooring line for example (A-D), is it still visible in the mooring section? In only part of it? To answer these questions, the correlations between the acoustic time series and different parts of the mooring line are calculated. The daily interpolated product described in the first chapter is used for the comparison.

For the correlation, the minimum and maximum longitude are incremented by steps of 0.5°, between 6.75°W and 8.75°E. For each range of longitudes, the range-depth-averaged

temperature is calculated over the first 1000m. The resulting time series is then compared with the acoustic data over the period 2010-12 and the correlation is calculated. These correlations are represented on the following figures for each acoustic path depending on the minimum and maximum longitudes used for the comparison with the mooring section.
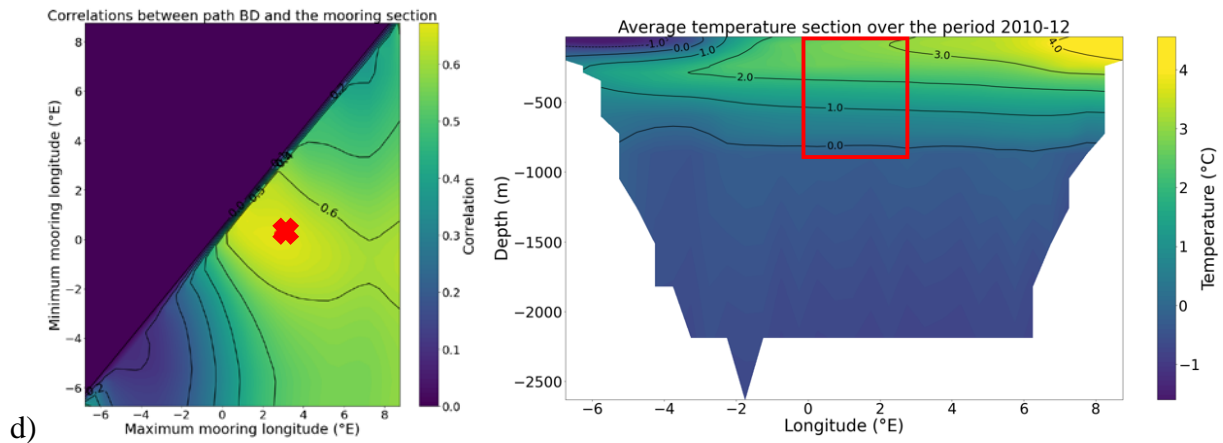
d)
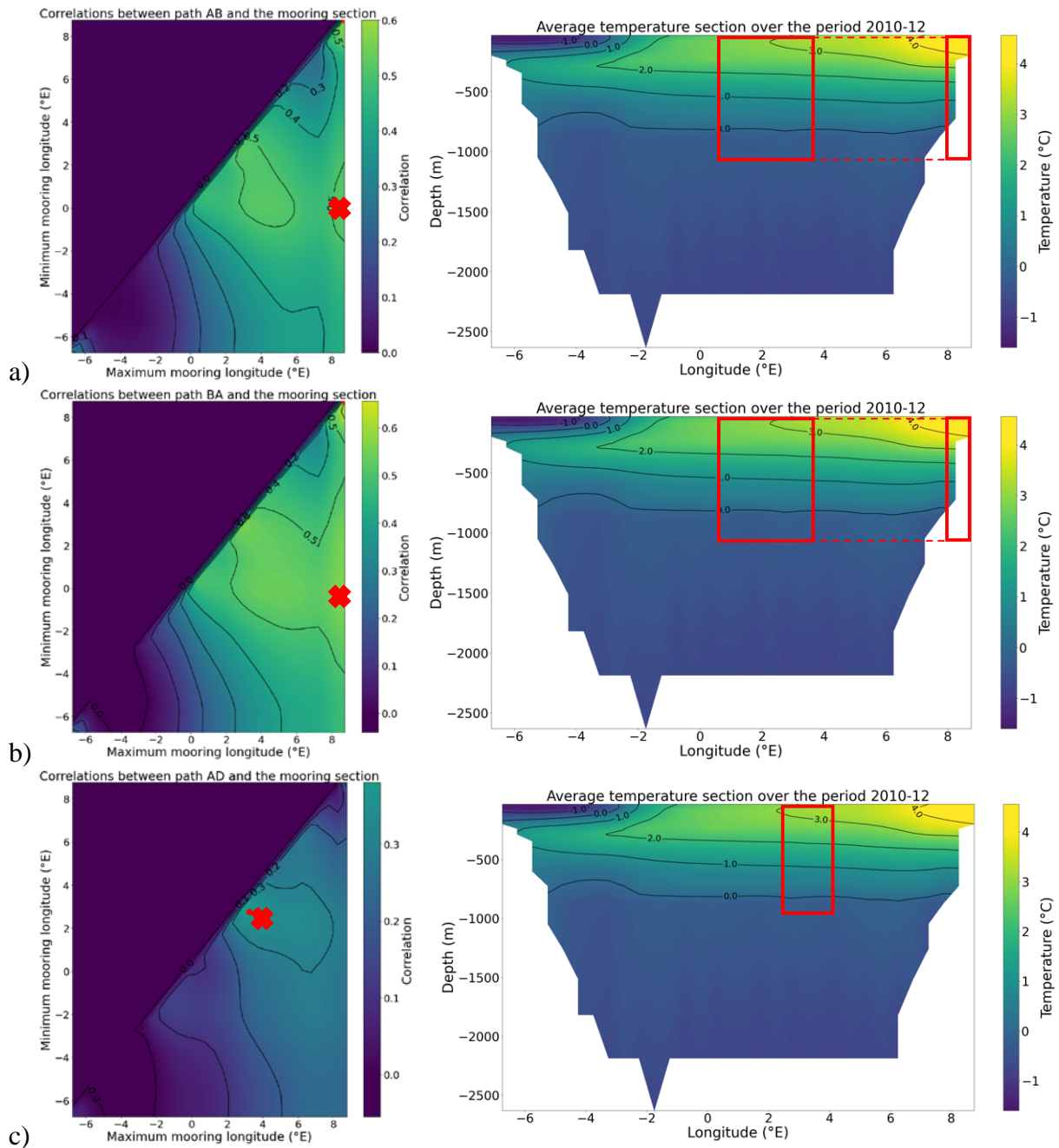
Figure 17: Correlations between the four acoustic paths (a) A-B, b) B-A, c) A-D, d) B-D) and the mooring section for all possible ranges of longitudes – left: the red dot indicates the maximum correlation and the red cross indicate the minimum and maximum longitudes kept for the following analysis – right: average temperature section between 2010 and 2012, the solid red boxes show the ranges of longitudes best-correlated with the acoustic path (a) A-B, b) B-A, c) A-D, d) B-D). The dashed boxes in a) and b) show the total range of longitudes that will be used in the later analysis of paths A-B and B-A.

Acoustic path	Best-correlated parts of the mooring section	Highest correlation
A-B	0°E - 4°E (central Fram Strait) 8°E - 9°E (WSC)	0.60
B-A	0°E-4°E (central Fram Strait) 8°E - 9°E (WSC)	0.65
A-D	2.5°E – 4°E (central Fram Strait)	0.38
B-D	0°E – 3°E (central Fram Strait)	0.67

Table 4: Maxima of correlation between the acoustic data and the mooring temperatures

The main outputs from the correlation analysis presented on Figure 17and Table 4 are as follows:

➢ Paths A-B and B-A, spanning over most of the Fram Strait south of the mooring line, are best correlated with the West Spitsbergen Current (8°E – 9°E) and part of central Fram Strait (0°E – 4°E), with maximum correlations between 0.5 and 0.6 The WSC and central Fram Strait will first be separately considered in the analysis, but we will then use the whole range of longitudes between 0°E and 8.75°E to compare sections of similar sizes and thus have a similar damping of local high-frequency events. Considering a larger section is also a way to ensure that no event responsible for the high correlation is missed.

➢ Path A-D, located in the east Fram Strait, is best correlated with the mooring line in central Fram Strait, between 2.5°E and 4°E, but the maximum correlation remains quite low (around 0.3). These low correlation values as well as the very low correlation with the WSC (0.2) need to be further investigated.

➢ Path B-D, located in the west Fram Strait, is best correlated with the mooring line further west in central Fram Strait (between 0°E and 3°E) and the maximum correlation is much

higher (between 0.6 and 0.7). We also note the very low correlation between B-D and the East Greenland Current, though both of them are located in the west Fram Strait.

4) <u>Discussion on the spatial correlations between the two datasets</u>

The acoustic data from the different paths are best correlated with specific parts of the mooring section. In this section, we try to interpret these results, starting with the asymmetry between paths A-D and B-D, and then addressing the region between A and B.

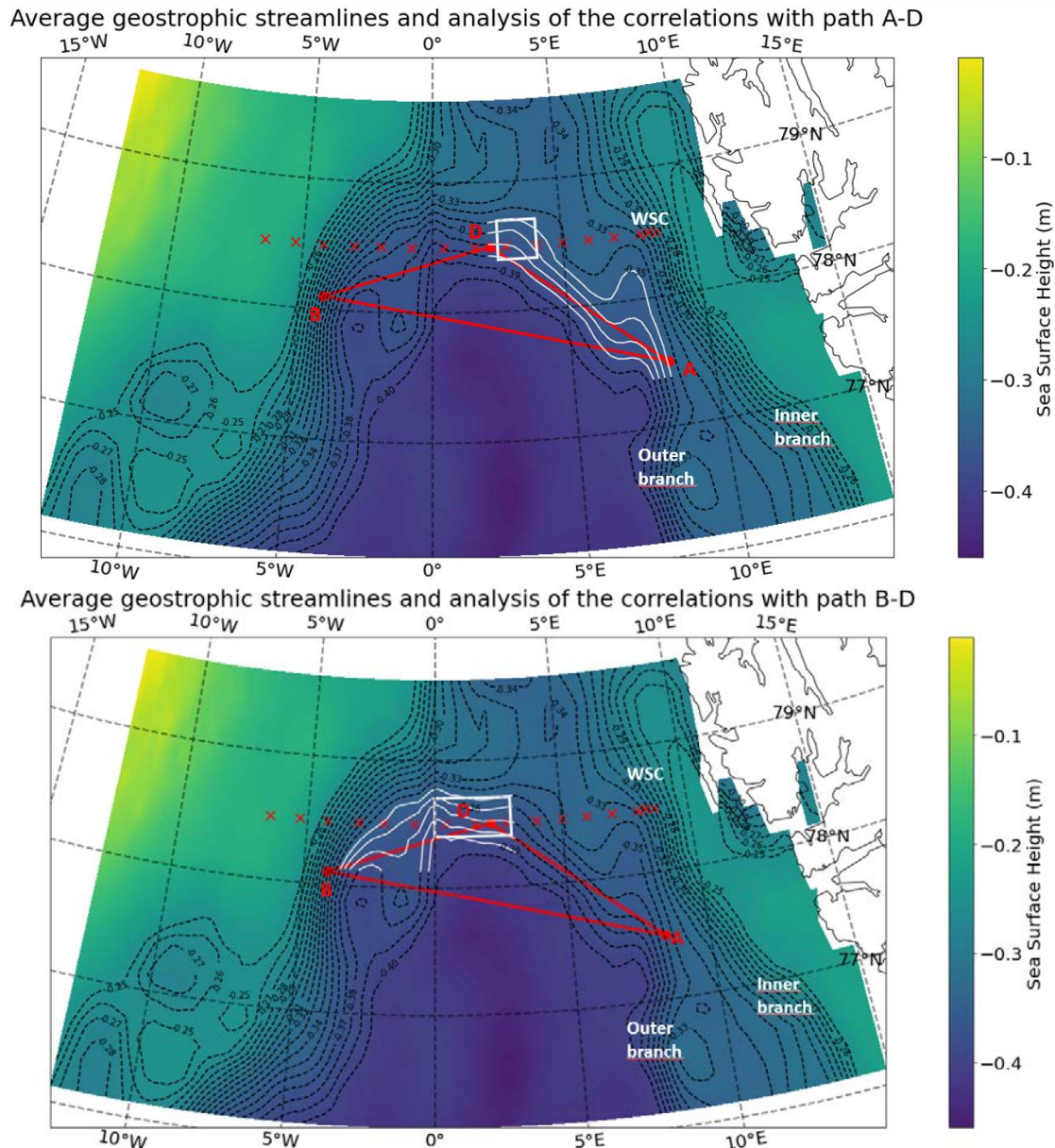*Figure 18: Mean sea surface height during the period of the ACOBAR experiment and derived streamlines of the geostrophic currents – the locations of the moorings and of the acoustic instruments are shown in red – the white boxes indicate the parts of the mooring line best correlated with paths A-D (top) and B-D (bottom) and the white streamlines show expected circulation paths between the mooring line and the acoustic paths.*

We use an altimetry dataset for the Sea Surface Height (SSH) available on CMEMS to have a broader picture of the average current pattern over the period 2010-12. The information provided by the geostrophic currents and their streamlines (derived from the SSH) is incomplete. However, the geostrophic currents obtained along the mooring line are qualitatively consistent with the average velocity section calculated from the mooring line, and we showed that the average currents in the Fram Strait were quite barotropic except in the EGC (also shown in [9]). We can thus use the geostrophic currents to estimate where the water masses found along A-D are expected to cross the mooring line and, conversely, where along the mooring line did the water masses found along B-D come from. These results are presented on Figure 18.

> ➢ We find that point A is almost located at the crossroads between the inner and outer branch coming from the Lofoten Basin and feeding the WSC and/or the recirculation branch. More precisely, A is closer to the outer branch, around 3° west of the main path of the inner branch. Following the average streamlines, the water masses found along path A-D can then be found in central Fram Strait, where the higher correlations were obtained. However, this result is also quite sensitive to any change in the location of the offshore branch of the WSC, and we note that the streamlines closer to point A first head north before recirculating west. In other words, water masses may follow a long and relatively complex path between A and the mooring line, which could explain the lower correlations with this path.
> ➢ The situation for path B-D is simpler. Though some of the water reaching B should probably come from the EGC, most of the locations along B-D can be traced back to central Fram Strait following the geostrophic currents. This is because the recirculation in this part of the Fram Strait mostly follows the mooring line before heading south.

We then check that the same method is also applicable to the interpretation of the results for paths A-B and B-A. This is done on Figure 19.
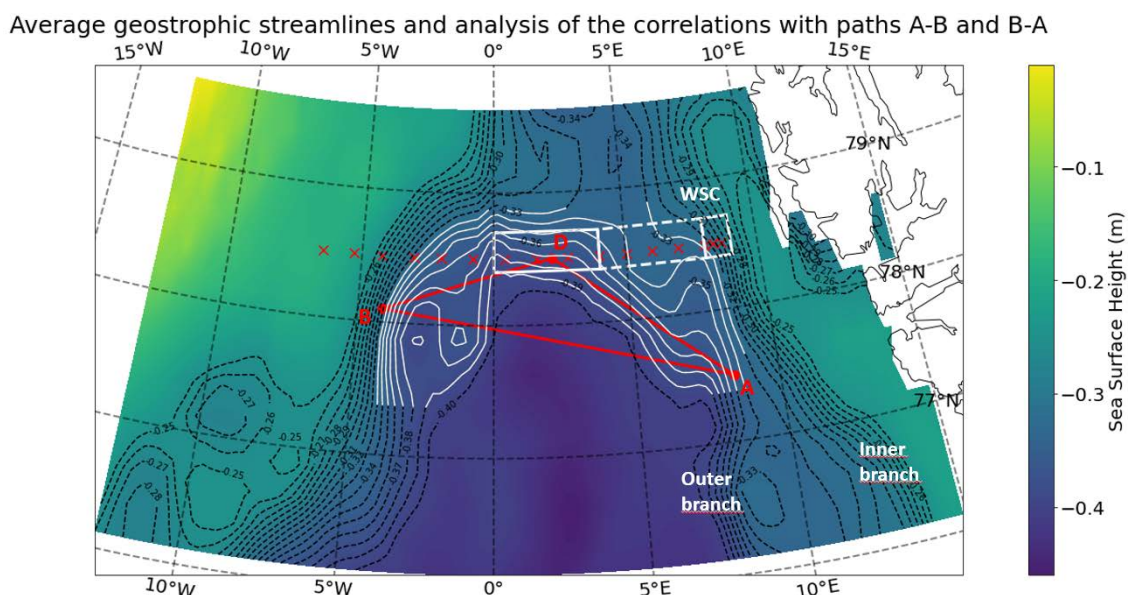

Figure 19: Mean sea surface height during the period of the ACOBAR experiment and derived geostrophic current streamlines – the locations of the moorings and of the acoustic instruments are shown in red – the solid white boxes indicate the parts of the mooring line best correlated with paths A-B and B-A, the dashed box shows the whole range of longitude

used in the comparison with the mooring data and the white streamlines show expected circulation paths between A-B and the mooring line.

Following the geostrophic streamlines, the main water exchanges between the region between A and B and the mooring line are as follows:

➢ Some of the waters found close to A head towards the WSC. Most streamlines are deviated just before the mooring line, but they suggest that these waters are still likely to join the WSC during some months.

➢ The waters located further west reach central Fram Strait west of 5°E, but there is no current streamline from A-B to the part of the mooring line between 5°E and 7.5°E, which is consistent with the local minimum of correlation found there.

➢ The waters located in central Fram Strait on the mooring line can be traced back to the eastern part of path A-B and the streamlines eventually meet path A-B again closer to point B. This could explain the high correlations between path A-B and central Fram Strait.

➢ Some waters from the EGC eventually reach point B.

Therefore, most of the correlations results obtained for paths A-B and B-A are consistent with the streamline analysis. More generally, the main outputs of the analysis on all four paths can be summarized as follows:

➢ The general correlations between the acoustic paths and the mooring data can be better understood thanks to the geostrophic currents.

➢ Point A is located on the outer branch coming from the Lofoten Basin. This branch mostly feeds the recirculating branch, but a few streamlines suggest that waters flowing past A may also sporadically join the WSC. Such variability might account for the low correlation values obtained with path A-D.

➢ Path B-D is located on a part of the recirculation showing less variability, which explains the higher correlations with the mooring line.

➢ The high-correlation between paths A-B and B-A and the WSC is not clear when looking at the streamlines. One explanation could lie in the stronger currents in this part of the section, which limit the heat exchanges with the atmosphere and allow for a better conservation of the water properties between the two latitudes.

All these interpretations indicate that, for all acoustic paths, the correlations between acoustic and mooring data mostly depend on the main circulation paths. As those tend to be quite instable, the correlations were also calculated over a shorter time period (3 months) to visualize these changes over the two years of the ACOBAR experiment. The results suggested that the correlations between the two datasets were quite variable in time, indicating changes in the main circulation patterns. However, the significance of such correlations was too low for the results to be conclusive.

Further analysis of the local circulation variability could involve the implementation of a lagrangian model following artificial drifters between the acoustic paths and the mooring line, which could complement and quantify these results. Yet this is beyond the scope of this work.

5) <u>Frequency analysis of the correlations</u>

We showed earlier (Figure 16) that the seasonal cycles were quite well-correlated between most acoustic paths and the mooring line. On the contrary, we do not expect small-scale high-

frequency eddies occurring at one location to be visible further north or south. Here we will thus study for which timescales the correlations between acoustic and mooring data are lost. To illustrate this difference between high and low frequencies, we first apply a 30-day moving average and calculate the correlations between the resulting time series.
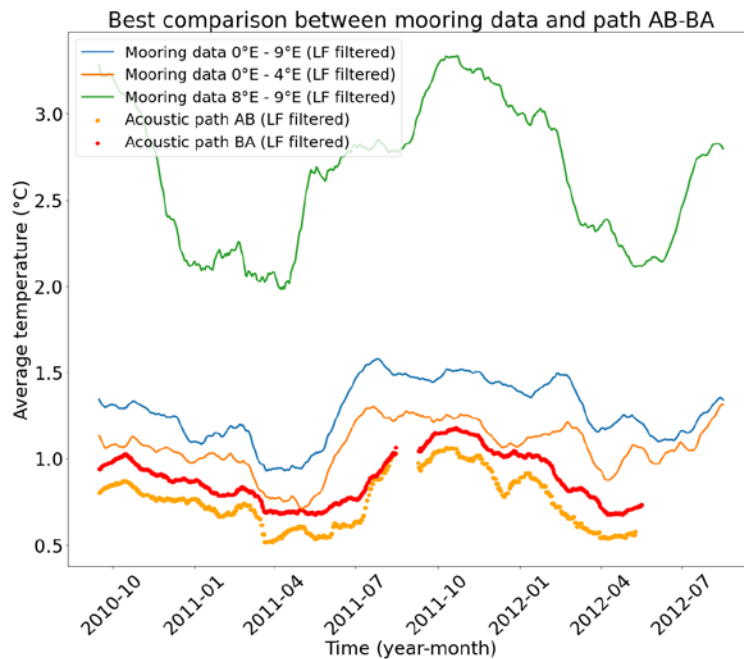

Figure 20: Low-frequency filtered acoustic time series on paths A-B and B-A and comparisons with filtered mooring data for different ranges of longitudes. All time series were filtered using a 30-day moving average.

Low-frequency correlations	Mooring data 0°E – 9°E	Central Fram Strait moorings (0°E – 4°E)	WSC moorings (8°E – 9°E)
Acoustic path A-B	0.75	0.73	0.77
Acoustic path B-A	0.78	0.73	0.85

Table 5: Correlations between paths A-B and B-A and different parts of the mooring section

We first compare acoustic paths A-B and B-A with the different parts of the mooring section with which they showed a good correlation: between 0 and 4°E in central Fram Strait, between 8 and 9°E in the WSC and the whole region between 0 and 9°E (Table 5). Low-frequency correlations between path A-B and B-A and both central Fram Strait and the WSC vary between 0.7 and 0.9. The difference between the correlations with the WSC and central Fram Strait can be partly explained by different temperature maxima in 2011 in the two regions. A late increase in temperatures is visible in the WSC during the autumn and the winter while temperatures are more regular in central Fram Strait throughout the second part of the year. We also note a general bias between acoustic and mooring data:

➢ The WSC waters are the warmest due to the presence of the warm current, but also because the shallow bathymetry does not allow to calculate the depth-average over the first 1000m.
➢ Central Fram Strait moorings are colder than the WSC but warmer than paths A-B and B-A, probably because of warm waters recirculating along the mooring line but not further south.

➢ There is an offset between paths A-B and B-A which is probably due to an instrumental bias in one of the acoustic sources.
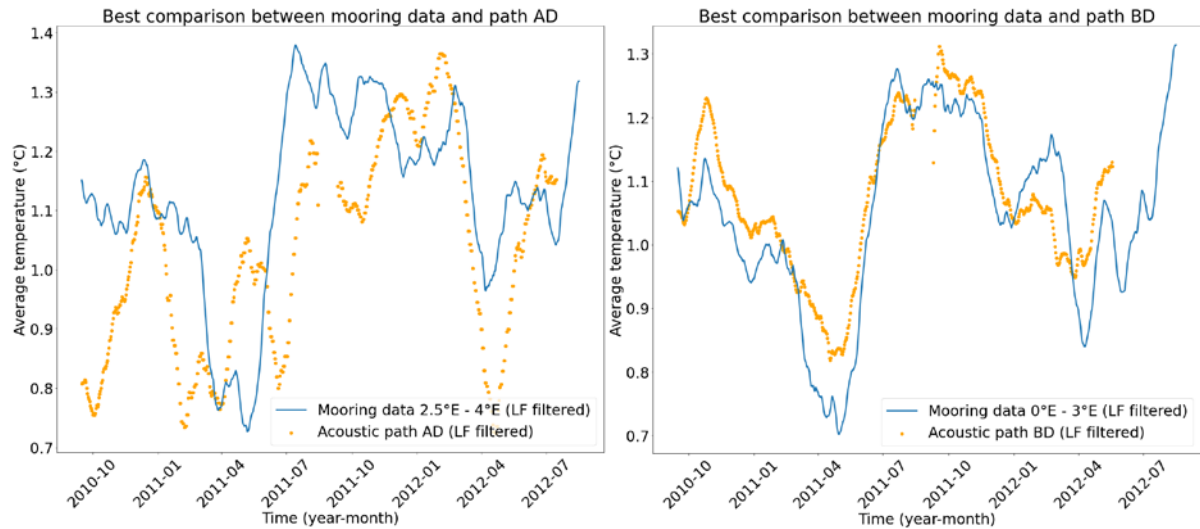

Figure 21: Low-frequency comparison between acoustic and mooring data for paths A-D (left) and B-D (right). Both time series were filtered using a 30-day moving average. The correlations are 0.54 for path A-D and 0.90 for path B-D.

We then consider the other two acoustic paths. On path A-D, the observed low-frequency variability has a more complex pattern than the seasonal cycle usually observed in the region. The large differences with the mooring data (in particular the cold minima in October 2010 or May 2012) confirm that A-D is not exactly located on the main recirculation path. As shown in the previous section, it is rather located at the crossroads between several currents.

On the contrary, the time series for path B-D confirms the good agreement between acoustic and mooring data.

The high-frequency part of the variability was also calculated by removing the low-frequency filtered signal from the initial time series. The corresponding figures are not presented here. However, the results show a clear loss of correlation for most paths (correlation between -0.05 and 0.1) except for path B-D which has a slightly higher high-frequency correlation of 0.20.

To determine more precisely for which frequency the correlations between both datasets are lost, we will now use band-pass filters on both acoustic and mooring data. Band-pass filtering the time series is not straightforward. Due to the gaps in the acoustic time series, the use of filters which would attenuate some frequencies in the Fourier transform of the signal is not possible. We thus opt for the use of two consecutive moving averages with different widths. The first one removes the high-frequencies, and the second one removes the low-frequencies from the resulting signal. The two timescales used here for each of the moving averages differ by 10 days.

We check the effective impact of these filters on the mooring data by calculating their gain as a function of frequency. The gain is defined as the ratio between the module of the Fourier transform of the filtered signal over that of the unfiltered signal. Figure 22 shows the results for two filters built with different moving-averages (and thus different expected cutting frequencies). In each case, the gain is maximum for the smaller of the two moving-average cutting frequencies.
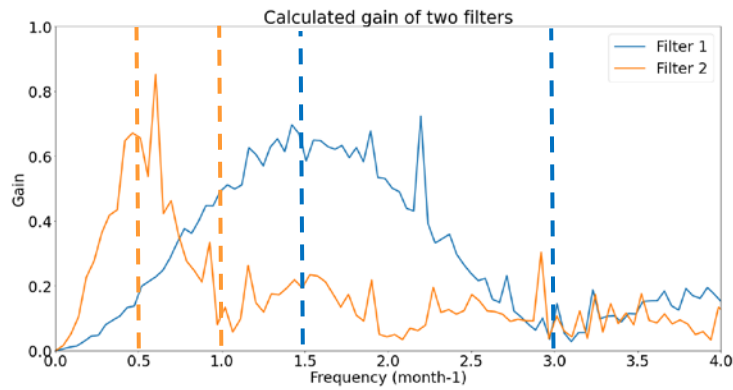
Figure 22: Calculated gains of two band-pass filters – the dashed lines indicate the inverse of the timescales of the two moving averages (1.5 and 3 months^{-1} for Filter 1 and 0.5 and 1 month^{-1} for Filter 2)
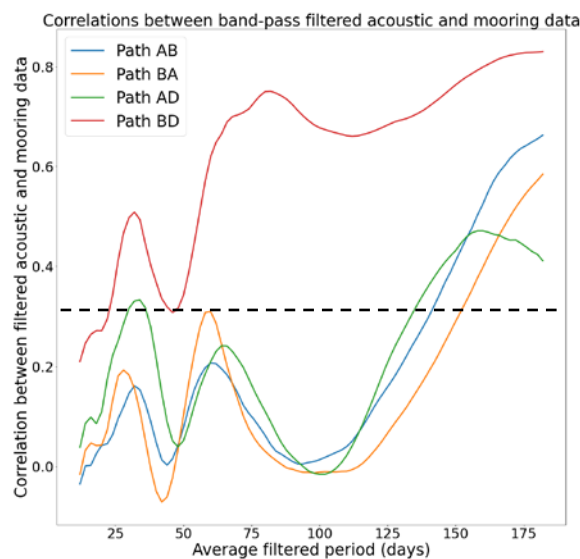

Figure 23: Correlations between acoustic and mooring data for all four paths as a function of the time periods considered for the filter – the dashed line indicates the minimum correlation value considered as significant (at p = 0.05)

After filtering both the acoustic and the mooring data with the filters described above, we calculate the correlations between both datasets for each range of frequencies (using the same ranges of longitudes as before for the mooring data).

Once more, B-D is by far the acoustic path showing the higher correlations, with all time scales longer than one month significantly correlated with the mooring line. For the other three paths, correlations are significant for time scales larger than four or five months. This result is not in contradiction with the significant low-frequency correlations previously found for all four paths with 30-day moving averages as all low-frequencies then contributed to the result.

We also note the local correlation maxima obtained on all four paths for time scales of 30 and 65 days (each of them being significant for two of the four paths). Such timescales are not easy to attribute to physical mechanisms as they are longer than usual eddies in the region (time scale of a week) and shorter than seasonal variations. They could be related to more complex variability in the current circulation, involving for example changes in the paths of the inner and outer branches coming from the Lofoten Basin and feeding the WSC or to variations of the main recirculation paths. Such hypotheses cannot be verified here, but these mechanisms were already identified as impacting the correlations between the two datasets in the previous section.

6) <u>Different behaviours at high frequency</u>

Though we showed that the high frequencies contained in the two datasets were not correlated, their relative importance compared to low frequencies is still worth analyzing. One motivation for the combined use of acoustic and mooring data was that they were expected to deal with high frequencies in different ways.

➢ Since the Rossby radius in Fram Strait is smaller than the distance between the moorings, some eddies may be completely missed when interpolating the mooring data. Yet, if an eddy's location coincides with a mooring location, the interpolation will spread the temperature anomaly caused by the eddy more than it should. Finally, when data was missing, only the low-frequency part of the signal was reconstructed, and the effect of eddies was not captured at all.
➢ On the contrary, in the acoustic dataset, all eddies encountered along an acoustic path are taken into account. But due to the small size of the eddies compared to the length of the acoustic paths, their influence on the result is also attenuated.

To compare the behaviour of both datasets regarding high frequencies, we compare their Power Spectral Densities (PSD). However, most acoustic datasets do not have temperature values for every day, so we focus on path BD which has both the highest data density and the highest correlation with the mooring line. The analysis is done on the first year of measurements, before the interruption in the data during summer 2011, with a particular focus on the period from September 2010 to April 2011 which is the longer period with uninterrupted daily acoustic data for B-D. It was however checked that similar PSDs were obtained when including the data from the second year of measurements. The results are presented on the figure below.
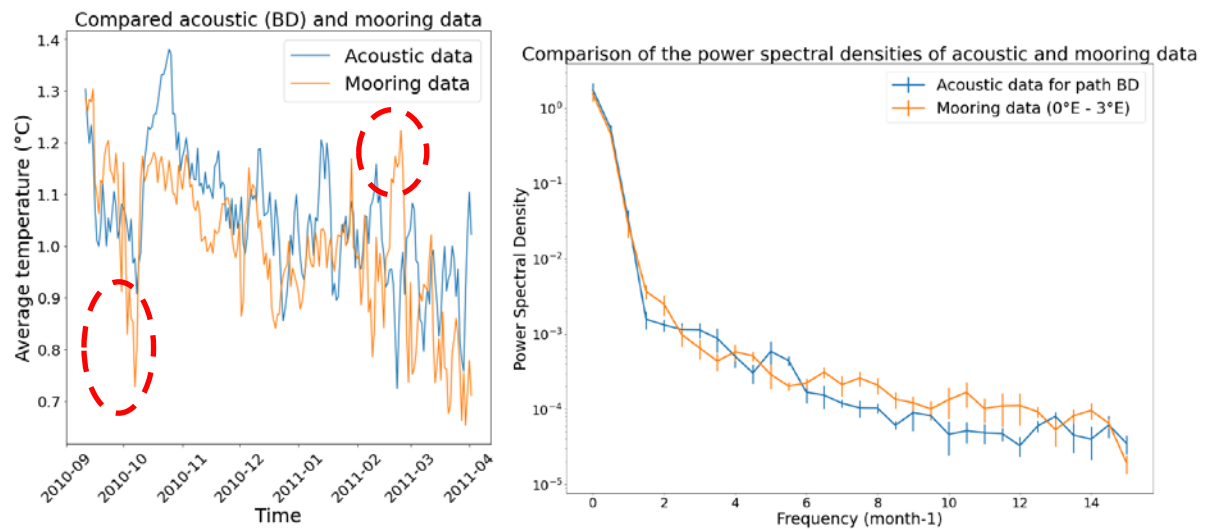

Figure 24: Comparison between the frequency spectra of acoustic path B-D and interpolated mooring data – left: Acoustic path B-D and mooring temperatures (0°E – 3°E) between 09/2010 and 04/2011 – right: Power spectral densities over the first year of the ACOBAR project.

The comparison shows that the amplitudes of the oscillations are comparable for both signals. A look at the spectra indicates that the PSDs for both signals are very similar for low frequencies. But for frequencies higher than 6 months^{-1}, the spectral density becomes consistently higher for the mooring data, with almost no overlap in the error bars between the two datasets. This result should however be tempered by the fact that the fraction of the mooring

section used in the comparison is of smaller size than the acoustic path, which reduces high-frequency attenuation.

The analysis of the circled parts of the figure, though uncertain, is consistent with the expectations. On the time series for the acoustic data, relatively regular oscillations with an amplitude close to 0.2°C and a period of a few weeks are visible. They could be induced by eddies forming on the acoustic path. On the mooring time series, most of the oscillations with a comparable frequency have a lower amplitude, except for two of them for which the amplitude is higher. This could be the result of the moorings missing most eddies while the interpolation amplifies the few eddies seen by the instruments. This is confirmed by the analysis of the detrended time series presented on Figure 25 and Table 6: only the mooring data shows oscillations exceeding 0.3°C while the acoustic data shows more oscillations with an amplitude between 0.15°C and 0.3°C.
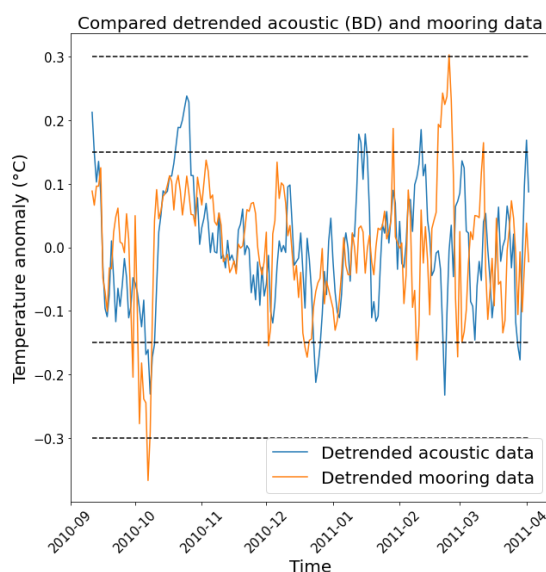

Figure 25: Detrended acoustic and mooring time series and comparison of the amplitude of the extrema – local extrema within a temperature range (0.15 to 0.3°C and above 0.3°C) are not considered

	Detrended acoustic data	Detrended mooring data
Number of extrema 0.15°C to 0.3°C away from the mean	12	9
Number of extrema beyond 0.3°C	0	2

Table 6: Classification of the extremum values of the detrended acoustic and mooring time series

A similar analysis was also carried out on the full time series available for B-D, showing consistent results but with a low significance. The present analysis should therefore be complemented by other approaches, which could include the use of high-resolution models, to confirm our hypotheses. One possibility would be to extract pointwise data from the model and test the effect of the interpolation algorithm on them. The errors generated during the interpolation process should then be representative of those induced by our interpolation of the mooring data.

7) Conclusions on the comparison between the two datasets

Throughout this chapter, we tried to understand the links that could be found between acoustic and mooring data, focusing on two aspects: the geographical correlations between different parts of the Fram Strait and the range of frequencies for which the observed correlations were valid. Though some of our assumptions would require further verifications, the main outputs can be summarized as follows:

➢ The two datasets are consistent with each other, both in terms of average values and amplitude of the seasonal cycle. Path A-B, located further south, is the only one not located on a recirculation path and thus has the lowest temperature.

➢ All acoustic datasets are better correlated with specific parts of the mooring line. These correlations are mostly significant for time scales longer than a few months and are always higher for path B-D.

➢ The average geostrophic currents show a very good consistency with the results of the geographical comparison. The best-correlated part of the mooring line can be linked to the corresponding acoustic path following the streamlines. So, acoustic measurements provide useful information on the main circulation paths over the first 1000m of the ocean.

➢ The amplitude of high-frequency oscillations is quite similar between the two datasets. However, the interpolation of mooring data seems to amplify artificially some small-scale temperature anomalies while missing others.

Most of all, this chapter highlights that the comparison between datasets of different natures can be pushed further than a simple consistency check. The fact that they cover slightly different areas is not so much a problem as a source of opportunities as we could demonstrate that the correlations between them are high enough to trace different water masses and circulation paths throughout the region. These results also provide an independent validation of the interpolation process detailed in the first chapter, which was found to capture some of the local – low-frequency - temperature anomalies in the Fram Strait with an amplitude comparable to integral acoustic measurements.

III. Model evaluation of TOPAZ-4b

1) Motivation and context

The availability of the interpolated mooring dataset, which was shown to be consistent with both CTD and acoustic observations, can be used to evaluate the model TOPAZ-4b, developed by NERSC. It is a coupled ocean-sea ice data assimilation system covering the region of the north Atlantic and the Arctic, using the ensemble Kalman filter (*Sakov et al, 2012*) [12][13], recently upgraded with higher vertical resolution (50 hybrid layers instead of 28 previously). In the model, the boundary conditions are implemented as a constant inflow through the Bering Strait and an outflow in the south Atlantic.

Since the Fram Strait is the only deep water connection between the Atlantic and the Arctic Oceans, the two main basins covered by TOPAZ-4b, it is a region particularly prone to error accumulation as many water masses from both basins eventually circulate there. To make it worse, the model resolution is between 12 and 16 km, which makes it eddy-resolving for low latitudes only. In the Fram Strait, the Rossby radius is only of a few kilometers and so the numerous eddies impacting the regional circulation and recirculations cannot be modelled properly. Wekerle et al, 2017 [19] have already demonstrated that using eddy-resolving models for the region significantly modifies both the larger scale temperature and velocity patterns. Finally, the partial sea ice cover in the Fram Strait throughout the year also adds to the complexity of modelling the region.

TOPAZ-4b assimilated all the remote sensing (SST, sea level, sea ice concentration, drift and thickness) and in situ data (temperature and salinity profiles) available on CMEMS, which does not include the AWI/NPI moorings. Our interpolated products can therefore be used to evaluate the reliability and performance of the model in the Fram Strait.

This chapter will focus on the evaluation of the water temperatures of TOPAZ-4b in the Fram Strait. We first describe the bias in the mean state and the temperature variability on a seasonal and interannual scale, then address the impact of data assimilation on range-depth averaged temperatures and finally discuss possible mechanisms which could be responsible for the observed errors.
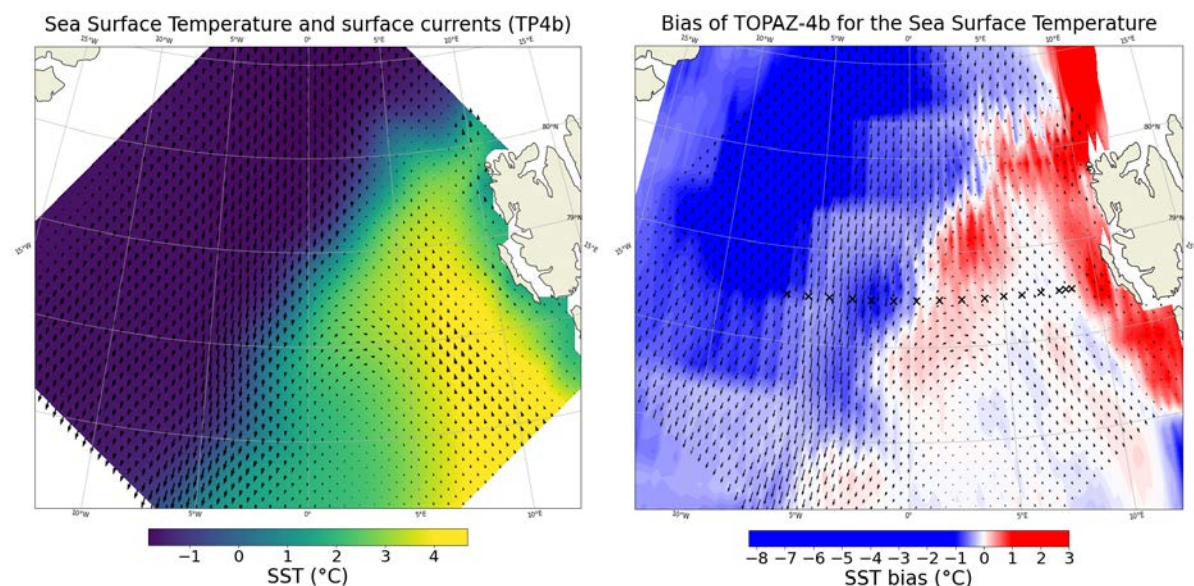
2) Biases in the mean state

Figure 26: Average surface temperature and currents between 1993 and 2016 from TOPAZ-4b (left) and temperature bias at the surface (right) – the black crosses indicate the location of the mooring line

As could be expected from a low-resolution model, the average surface current pattern, presented on Figure 26, is simpler than that obtained from altimetry data (see previous section). Only one main branch is visible for the WSC, and the recirculation pattern, mostly located between 77.5°N and 78.5°N, has a very simple structure. The temperature bias is calculated using the SST satellite measurements available on CMEMS. The surface WSC has a low temperature bias south of the mooring line (smaller than 0.5°C) but becomes too warm further north and next to the coast of Svalbard. There is also a warm bias in central Fram Strait along the mooring line east of 0°E, and then a cold bias in western Fram Strait. Since western and

central Fram Strait are partially covered with ice for most of the year, such biases are probably very much influenced by the regional sea ice cover in the model.

The temperature bias along the mooring section is then calculated using the monthly interpolation product, which was obtained combining both mooring and satellite SST data. The result is shown on Figure 27 below.
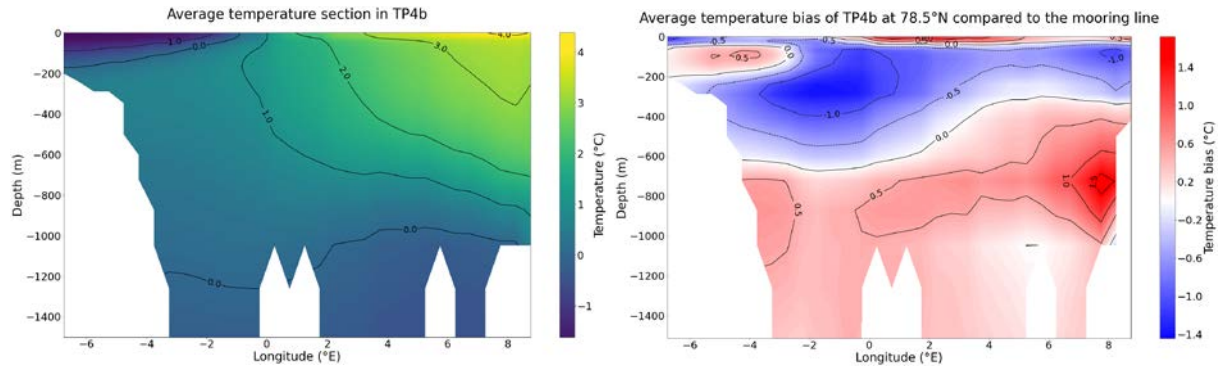

Figure 27: Average temperature section from TOPAZ-4b at 78.5°N (left) and bias compared to the interpolated mooring data (right)

In central and eastern Fram Strait, the warm bias that was observed at the surface disappears after a few tens of meters and is followed by an important cold bias spanning over all of the Fram Strait until 700m deep in the west and 500m in the east. This layer of water can be as much as 1.2°C too cold, which is significantly more than the uncertainty on the result of the interpolation. Deeper waters then display another warm bias until the ocean bottom, with the highest values reached around 800m deep below the WSC (up to 1.6°C too warm).

In other words, the vertical structure of the WSC is not captured very well with the warmest waters located too close to the surface but also extending too far deep and warming too much the water masses (Arctic Intermediate Waters) located below. Besides, the warming of the recirculating branch is not strong enough as warm Atlantic waters should still be present in the subsurface much further west, even below the cold EGC.

Since the temperature section in the Fram Strait is influenced by the local circulation, the average velocity sections from TOPAZ and the mooring data are also compared on Figure 28.
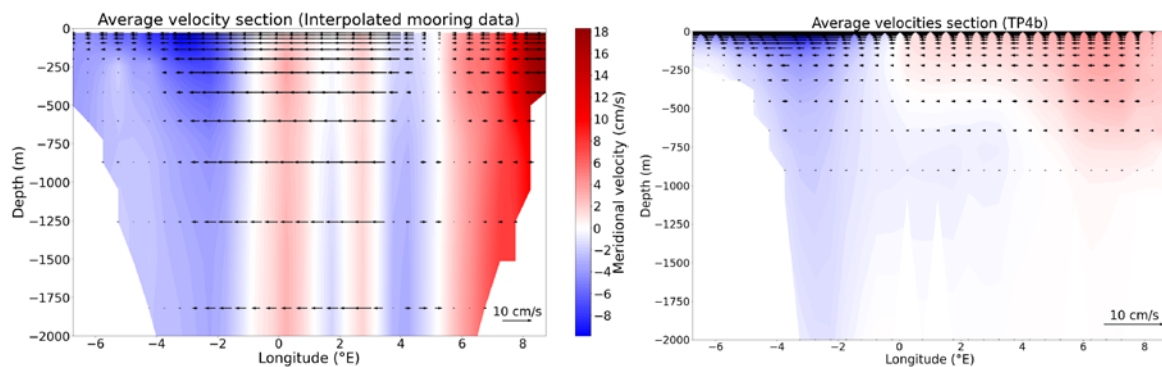

Figure 28: Average velocity sections from mooring data (left) and TOPAZ-4b (right) – the colors represent the meridional currents (positive northwards – identical color scale for the two figures) while the arrows represent the zonal currents

The errors made by TOPAZ in the currents are more pronounced than the errors in the temperature section. Beyond the simplification of the general recirculation pattern, it can be seen that TOPAZ largely underestimates the intensity of the WSC (up to a factor 4) and that all currents are limited to surface and subsurface waters while observations show a much more

barotropic structure. The Fram Strait currents in TOPAZ-4b therefore face three main issues: a simplified horizontal structure, an underestimated intensity of the WSC and an absence of deep currents. These errors impact the mean temperature section, but the distinction between warm waters in the east and cold waters in the west is nevertheless captured.

3) Temperature variability in TOPAZ

In this section, we analyze the model's ability to replicate the temperature variability in the Fram Strait. The power spectral densities of the range-depth averaged temperatures are used to extract the main frequencies of the variability and compare their relative contributions to the total signal. The results are presented on Figure 29.
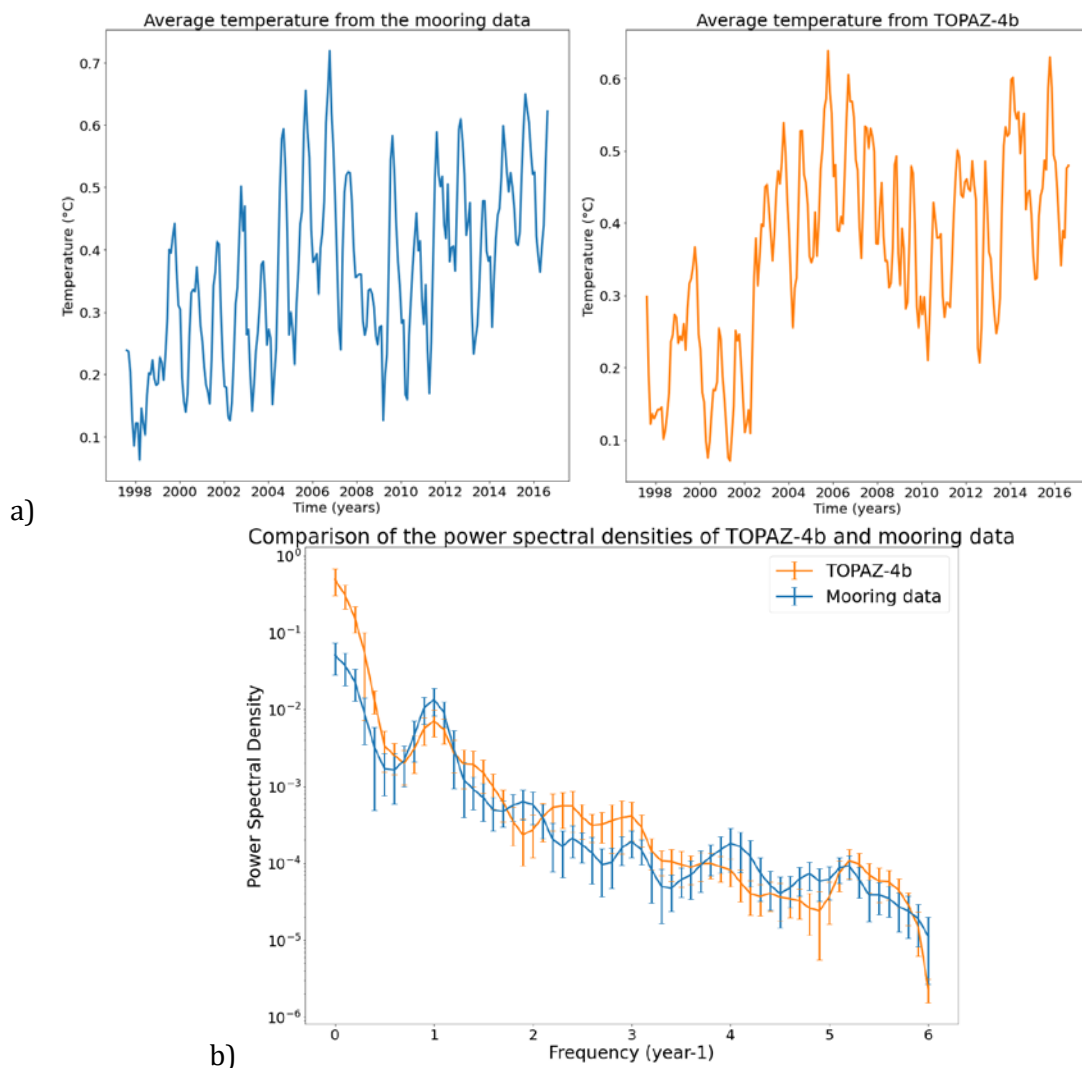
Figure 29: a) Time series of the range-depth averaged temperatures (6.75°W to 8.75°E between the surface and 2000m) obtained from the interpolated mooring data (left) and TOPAZ-4b (right). b) Power-frequency spectra of the average interpolated temperature and of the average temperature section from TOPAZ-4b

The main difference visible in the spectra is the relative amplitude of the seasonal cycle compared to lower frequency variability: TOPAZ-4b tends to overestimate the importance of interannual variability while underestimating the seasonal cycle compared to observations. In the corresponding time series, this is reflected by a more irregular seasonal cycle in TOPAZ

and a drastic temperature increase in 2003 in anticipation of the 2006-07 warm anomaly. The latter could possibly be related to the introduction of new technology (the Argo buoys), which assimilation could have caused discontinuities in the reanalysis as will be explained later.

The effects of the temperature seasonal cycle can be analyzed further, considering first the variability of the range depth average temperature and then identifying the influence of the different water masses.
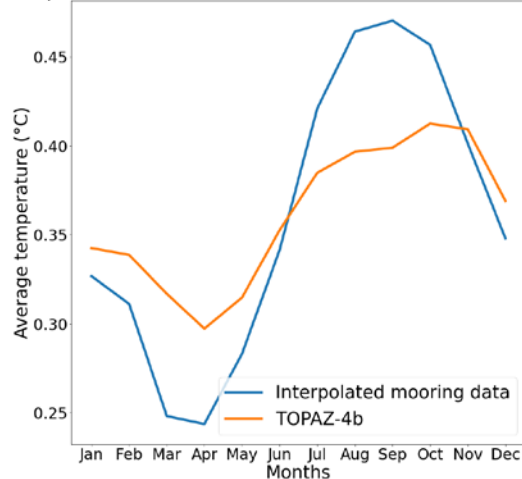
Model / Observations	Average temperature (°C)	Amplitude of the seasonal cycle (°C)
Interpolated mooring data	0.360	0.227
TOPAZ-4b	0.361	0.115

Figure 30: Comparison of the average temperature seasonal cycle temperatures (average from 6.75°W to 8.75°E between the surface and 2000m)

Table 7: Average temperature and amplitude of the seasonal cycle in TOPAZ and the observations

The main outputs of the range-depth averaged seasonal cycle comparison are the following:

➢ The average temperature is similar in TOPAZ and the observations, as the the warm bias below 700m is compensated by the cold bias above.
➢ The amplitude of the seasonal cycle is underestimated, which is consistent with the relatively weak amplitude observed in the power-frequency spectrum compared to low frequency variability.
➢ Both seasonal cycles reach a minimum in April, but TOPAZ reaches its maximum in October, one month later than in the observations. In November, temperatures in TOPAZ remain relatively high instead of going down.

It is also possible to have a synthetic spatial vision of the impact of the seasonal cycle on the mooring section. We subtract the mean and normalize the seasonal cycles to create an index on which regressions of the temperature sections are performed. The results of the regression for TOPAZ and the observations are presented on Figure 30.
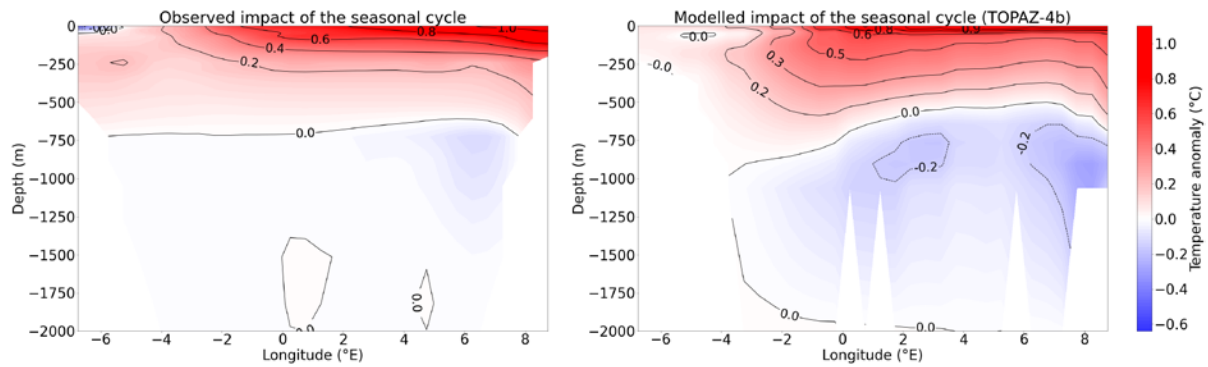
Figure 31: Observed (left) vs modelled (right) impact of the seasonal cycle on the temperature section – the temperature anomaly corresponds to the temperature variation induced by a variation of 1 of the index defined from the seasonal cycle

Both the observations and the model show quite similar patterns close to the surface, with most variations occurring in eastern and central Fram Strait in the first 500m. The surface variations are slightly more intense in the observations, but the anomaly extends deeper in western Fram Strait in TOPAZ. Around 750m, the temperature anomaly switches sign: deep waters are warmer in winter and spring than during the summer. This phenomenon seems to have a stronger impact on TOPAZ where the opposition between subsurface and deeper waters is more pronounced. This also provides an explanation for the lower amplitude of the depth-averaged seasonal cycle in TOPAZ, since subsurface and deep water variability partially compensate each other. Though the seasonal cycle has a clear impact in the WSC and the recirculation branch, the EGC stays mostly unaffected, with no visible warming during the summer. This region is never completely ice free, which forces the surface temperature to remain close to 0°C.

We proceed in a similar way to study the interannual variability, using the time series of the temperature anomalies from the seasonal cycle.
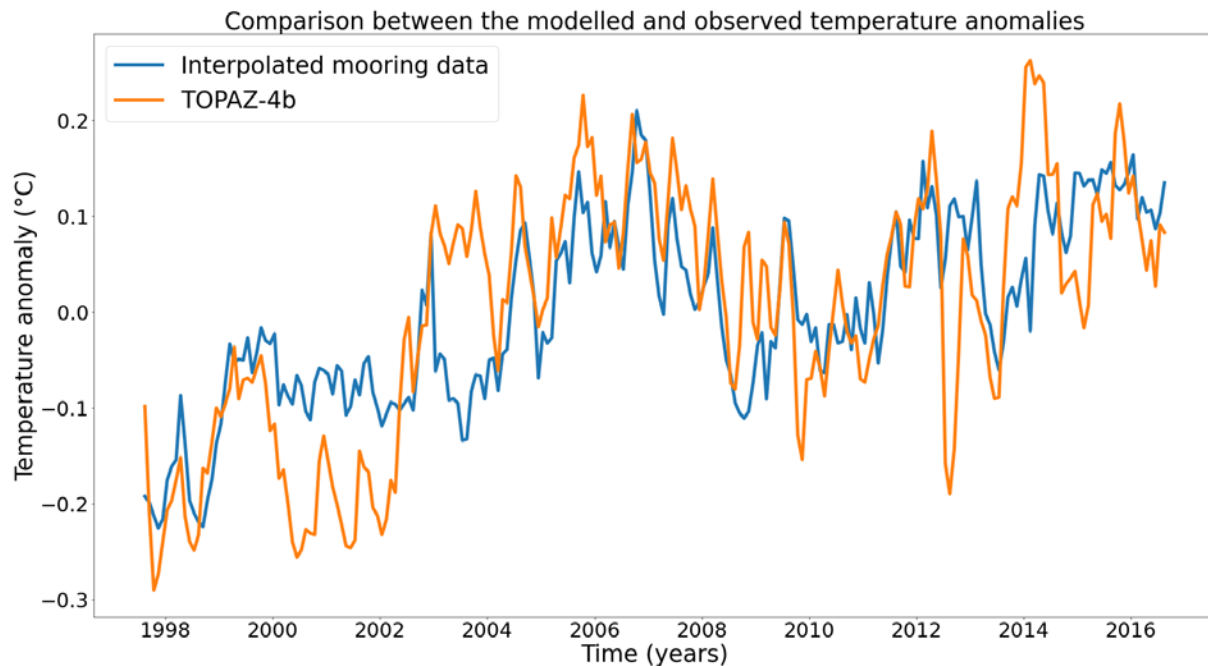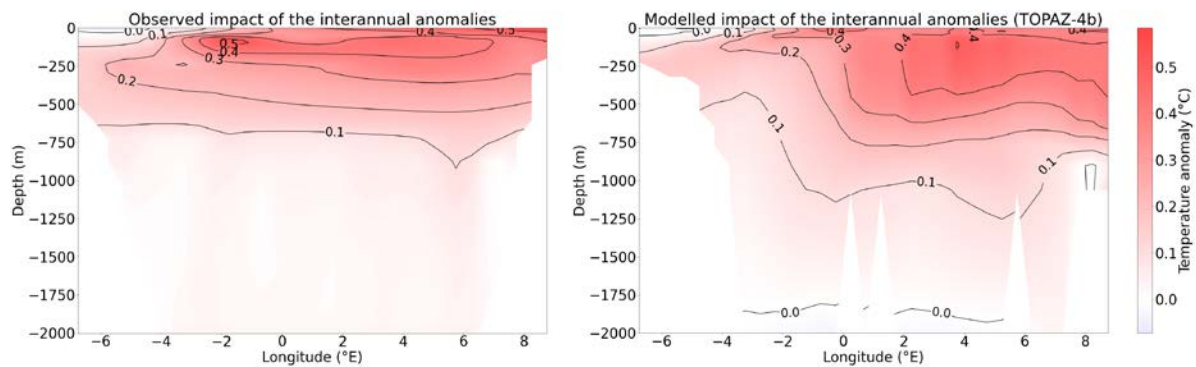

Figure 32: Comparison of the temperature anomalies from the seasonal cycle between the model and the observations (averaged between the surface and 2000m, from 6.75°W to 8.75°E) – the correlation between the two time series is 0.73

The trend of global warming is visible on both time series, with an average temperature increase of 0.013°C/year in the observations and of 0.014°C/year in TOPAZ. The most obvious patterns of interannual variability, like the warm anomaly in 2006-07, are also always present. However, the time series for TOPAZ-4b shows more variability over time scales of one or two years.

As was done for the seasonal cycle, the previous time series are normalized to define an index which is used to visualize the spatial patterns related to interannual variability and global warming.

Figure 33: Observed (left) vs modelled (right) impact of the low-frequency variability on the temperature section – the temperature anomaly corresponds to the temperature variation induced by a variation of 1 of the index defined from the time series of the temperature anomalies

The amplitude and patterns of the variability are once more quite similar between TOPAZ and the observations: interannual anomalies tend to have a deeper extent and tend to affect subsurface and intermediate waters both in eastern and central Fram Strait. Contrary to seasonal variability, interannual variability warms and cools subsurface and deep waters simultaneously. A few differences between TOPAZ and the observations are however visible:

- ➢ There is a stronger east-west asymmetry in TOPAZ which could be related to the poor representation of the west of the recirculation branch.
- ➢ In eastern and central Fram Strait, the anomalies extend to deeper waters in TOPAZ compared to the mooring data. For example, the 0.2°C isoline is 800m deep instead of 500m deep in TOPAZ in eastern Fram Strait.
- ➢ Bottom waters in TOPAZ (below 1800m) do not show any warming trend.

All in all, TOPAZ-4b has relatively strong biases in the mean temperature and current patterns but is nevertheless able to replicate the impact of both the seasonal cycle and the interannual variability in the Fram Strait.

4) Contribution of data assimilation (DA)

Since the temperature anomalies in the Fram Strait were shown to be driven by changes in the intensity of the local circulation (Chatterjee et al., 2018), these results may seem surprising. The explanation lies in the use of data assimilation (DA), which relies on remote sensing and in situ measurement to correct the state of the modelled ocean every seven days. We describe here how DA affects the average modelled temperature in the Fram Strait.

The mooring line is divided in two parts, east and west of point D – the acoustic receiver - located at 2°E. This is done to compare the impact of data assimilation on locations where different observational data is available: since western Fram Strait is mostly covered with ice throughout the year, it is not as much explored as the eastern part of the strait during

oceanographic campaigns and fewer in situ measurements are available. Figure 34 compares modelled and interpolated range-depth averaged temperatures over the first 1000m in both parts of the strait over the period 2010-12, already analyzed in the previous chapter. The choice to restrict the analysis to the first 1000m is justified by both the larger variability in this layer and the inversion of the seasonal cycle in deep waters.
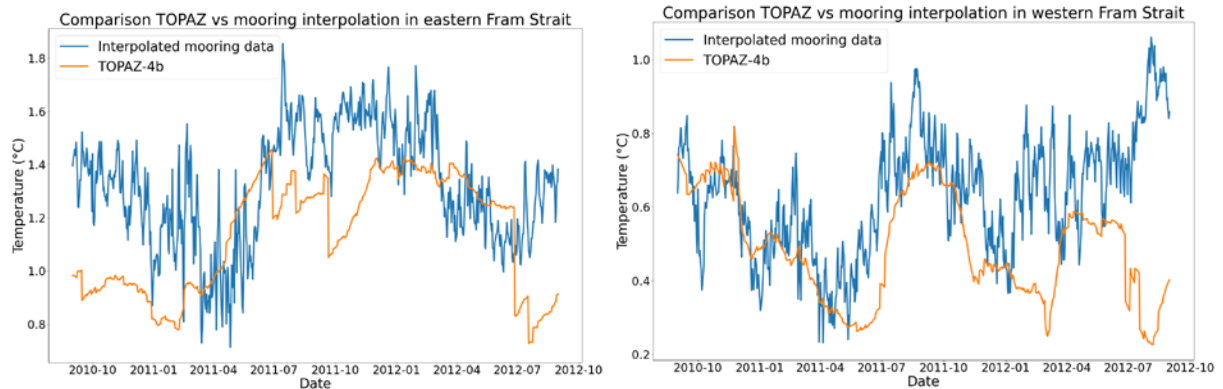

Figure 34: Comparison of the daily temperature time series in eastern (6.75°W – 2°E) and western (2°E – 8.75°E) Fram Strait from the mooring data and TOPAZ-4b – temperatures are averaged over the first 1000m of the ocean.

As can be expected from a low-resolution model, Figure 34 shows that high-frequency oscillations in TOPAZ are strongly attenuated compared to mooring data. But mostly, the impact of the DA steps occurring every seven days becomes clearly visible. In July 2011 in eastern Fram Strait for example, they are reflected by the presence of regular steps in the TOPAZ time series. These steps can be as large as 0.2°C, which is half the total amplitude of the seasonal cycle. Therefore, a single DA step may be enough to generate a strong – and potentially lasting – anomaly. In some instances, one step seems to alter the average temperature in the Fram Strait for several months. A good illustration is the sudden drop in temperatures observed in July 2012 with TOPAZ but not the mooring data: in both eastern and western Fram Strait, the average temperature was suddenly reduced by several tenths of degrees at once when some data was assimilated. As a result, no summer maximum was visible this year in the TOPAZ data.

The assimilated datasets are all taken from CMEMS. They include altimetry data and remote sensing throughout the year, but also in situ data, mostly available during the summer when oceanographic campaigns are possible in the Arctic. In particular, in situ data like CTD measurements are likely to induce corrections over the whole water column and thus affect more the depth-averaged temperatures, which is consistent with the largest steps being obtained in eastern Fram Strait during the summer.

The previous observations can be extended to the whole study period (1997-2016) using statistical analysis. More precisely, we consider the seasonal cycle of the temperature corrections induced by data assimilation. From the time series of the average temperatures, we isolate the days where DA was performed by sorting the data by differences between consecutive days and keeping the highest values for each month ($1/7^{th}$ of the data). The data is represented using box plots to highlight the presence of outliers.
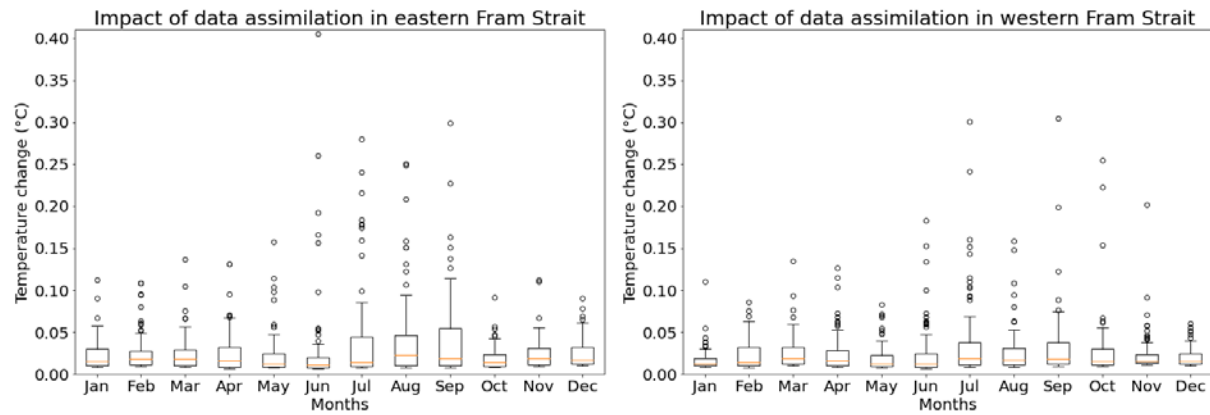
Figure 35: Impact of data assimilation steps on range-depth averaged temperatures over the first 1000m depending on the month – left: in eastern Fram Strait – right: in western Fram Strait

Figure 35 confirms the observations made over the period 2010-12. DA has a stronger impact in summer months (particularly between July and September) and in eastern Fram Strait. More importantly, it shows that the number of outliers with values higher than 0.15°C is larger than the number of years in the time series. So, more than once a year, the Fram Strait temperatures are modified by more than half the amplitude of the seasonal cycle by a single DA step.

In the end, DA plays a crucial role in the model as it allows to capture most of the temperature variability despite important biases in the mean state. But due to the irregularity of the assimilated datasets, pointwise data may generate sudden temperature changes in the whole section and cause new errors. In the next section, we propose explanations and suggestions to improve on the identified issues of the model.

5) Discussion and interpretation of the observed errors

a) *Interpretation of the biases in the vertical structure*

The horizontal resolution of the model as well as the baroclinicity of the WSC were already identified as possible improvements for TOPAZ. They may help obtain a more realistic circulation pattern but would probably not affect the biases of the model in the vertical structure. To understand where these come from, it can be interesting to analyze further one of the previous results: the inversion of the seasonal cycle between subsurface and deep waters. The normalized average seasonal cycles for several depths are plotted on Figure 36 with both the mooring and TOPAZ data.
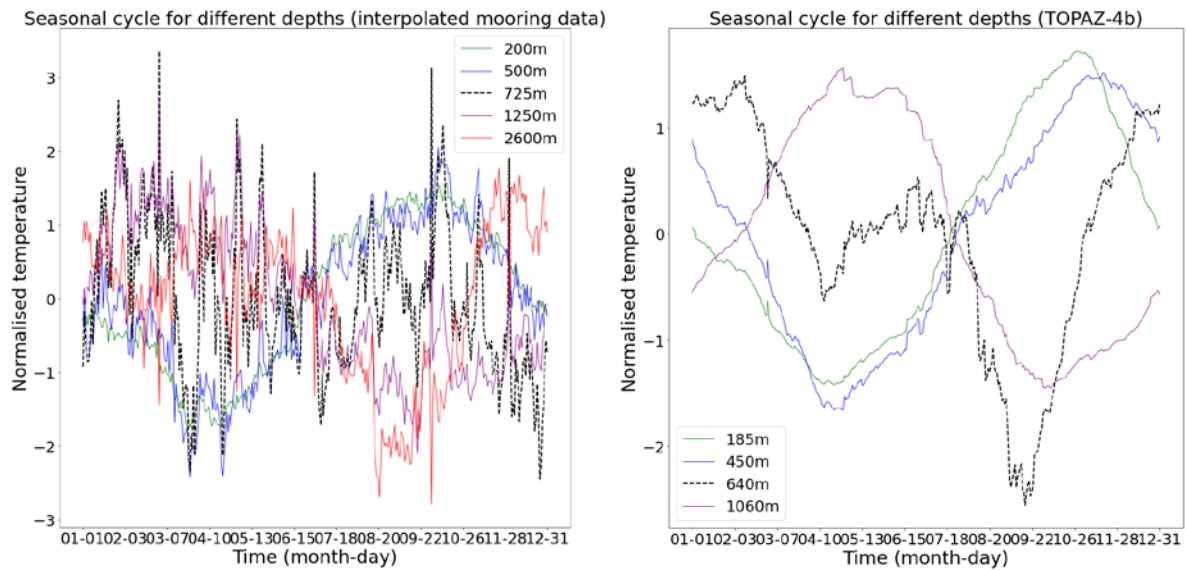
Figure 36: Average normalized temperature seasonal cycles for different depths, calculated from the daily interpolated mooring data (left) and the daily output of TOPAZ-4b (right)

In both cases, the switch occurs around 750m where the mooring data almost does not have a seasonal cycle anymore. Vertical mixing is probably involved in this inversion. During the summer, the subsurface warms and becomes fresher due to sea ice melt. It increases the stratification and the heat is confined to the surface. In the winter however, subsurface waters cool down and become more saline and stratification is weakened. Part of the remaining heat is then transmitted to deeper waters, which explains the seasonal cycle inversion.

We showed that this inversion tends to be overestimated in TOPAZ, which could point at a more general overestimation of vertical mixing by the model in the Fram Strait. This could originate in the mean temperature biases identified in TOPAZ by warming deep waters at the expense of subsurface waters. It can be shown from our interpolation of subsurface salinity that TOPAZ has a small positive salinity bias close to the surface throughout the year. Combined with too cold subsurface waters, this creates a positive density anomaly above 750m and should induce even more vertical mixing. In other words, a small overestimation of vertical mixing generates a positive feedback loop which could be responsible for the mean temperature biases. This interpretation is consistent with the fact that both the cold and warm biases are maximum in spring (when the stratification is lower) and minimum in autumn. The mean temperature biases for April and October are presented on Figure 37.
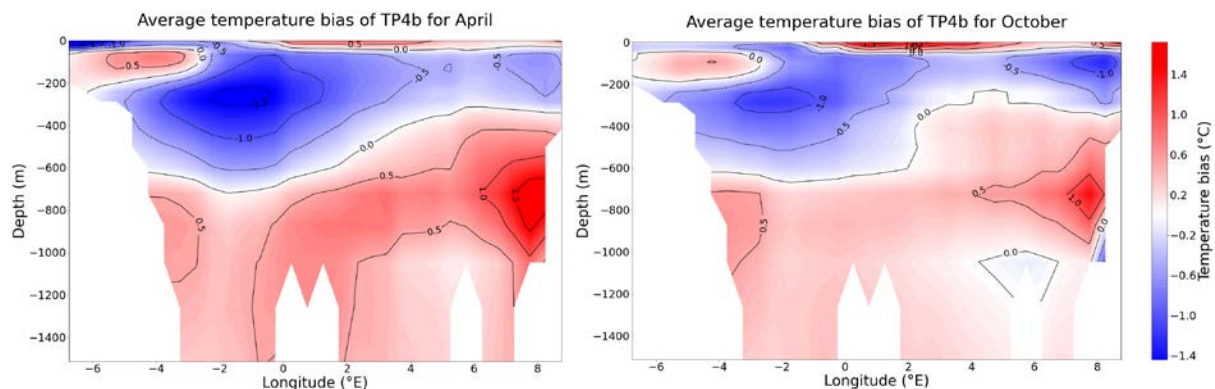

Figure 37: Average temperature bias of TOPAZ-4b for April (left) and October (right)

b) <u>*What happens to DA-induced errors*</u>

The consequences of DA, though described and quantified in the previous section, need to be further understood. The assimilation of a single dataset can induce large variations over a single day, and the analysis of the curves of Figure 34 shows that this sudden variation does not always reduce the error. For example, CTD measurements performed at one location may not reflect the overall temperature anomaly in the Fram Strait because of the presence of multiple small-scale eddies, and some of them could induce errors if no simultaneous observations in other parts of the strait are available.

Going further, one could wonder whether the model spontaneously corrects such DA-related errors after a few time steps. In the real Fram Strait, local temperature anomalies are expected to be short-lived as they would be advected by currents both close to the surface and in deep waters. But in the model, the underestimation of the WSC intensity and the absence of deep currents could mean that local anomalies and errors remain longer in the Fram Strait. On Figure 34 (time series), a sudden drop in temperatures is visible in eastern Fram Strait in September 2011. It matches a brief temperature drop in the observation time series, before temperatures rise again two weeks later and stay high throughout the winter. However, this DA step comes at the end of the summer season, and fewer in situ measurements are available in the following months. The average temperature in TOPAZ thus rises again, but very slowly, and only stabilizes three months later in December.

This example shows that part of the errors made by TOPAZ most likely result from complex interactions between initial biases in the modelled ocean and DA steps.

6) <u>Recommendations to reduce the errors</u>

From the previous analysis, several suggestions can be made to improve the results of the model in the Fram Strait.

➢ Increasing the horizontal resolution: it has been shown that if a model becomes more eddy-permitting (or even eddy-resolving) in the Fram Strait, the complexity of the circulation pattern should become visible [19], with several distinct branches for most currents. Eddies may also be generated around small-scale bathymetric features like the Molloy hole, and we can expect to replicate better the complexity of the recirculation patterns. Increasing the model resolution remains however curtained by computational limitations.

➢ Investigating the impact of the parameters involved in wind-ocean interaction and friction at the ocean bottom. We showed that the main currents in TOPAZ are confined to the surface while observations indicate a more barotropic structure. In TOPAZ, the barotropic and baroclinic components of the currents are calculated separately before being merged, and the barotropic component mostly responds to interactions with the wind and the ocean bottom. Strong currents close to the ocean bottom should increase the influence of the bathymetry which is expected to be quite strong at high latitudes. Moreover, a deeper extension of the WSC might help correct the cold anomaly observed in the subsurface until 500m deep.

➢ Perfecting the parametrization of vertical mixing: too strong mixing could be an explanation for some of the observed biases (too cold subsurface waters and too warm deep waters). Those biases are then self-maintaining as they reduce the stratification.

➢ Assimilating the data from the AWI/NPI moorings. The abrupt corrections induced by DA during the summer mean two things. First, the model tends to drift quickly away from the observations. This issue could be partially addressed by the above suggestions. Second, the irregularity of available data makes some assimilations steps much more important than others. By providing in situ data throughout the year, the moorings could be used to solve part of this problem and help us replicate better the complex structure of the Fram Strait section. The acoustic measurements from the ACOBAR project could also be assimilated as they also provide continuous information on subsurface waters over a 2-year period.

IV. Understanding the temperature and circulation variability and trends from the Nordic Seas to the Barents Sea

1) Introduction

The first three chapters of this report were organized around the interpolation of the Fram Strait mooring data and several possible applications. The main motivation for investing in the deployment of instruments in the Arctic is to understand the changes happening in the region. In particular, the datasets show that the temperature variability in the region features strong interannual anomalies (for instance in 2006-07) and a clear warming trend. Here we will study the mechanisms driving this variability and consider the Fram Strait in the wider context of the Nordic Seas. For most of the analysis, we will leave the mooring data aside and work with remote sensing data and atmospheric reanalyzes. However, the impacts on the Fram Strait and the question of the consistency of our results with the mooring data will eventually be addressed.

We will show that, despite the water fractionation between the water masses entering the Barents Sea or heading towards the Fram Strait (Broomé et al., 2021 [3]), changes in circulation paths over the Nordic and Barents Seas are eventually linked to each other. We will combine altimeter data and in situ observations to understand the main mechanisms causing the circulation anomalies in the Nordic Seas and the Barents Sea, on both the interannual time scale and as a response to global warming. The choice of including both regions is relevant for two reasons: (1) to highlight the differences in the driving mechanisms in the two regions; and (2) due to the fact that they are connected via the Barents Sea Opening (BSO) and the formation of Arctic Intermediate Waters in the Barents Sea flowing through the Fram Strait below the West Spitsbergen Current (WSC). We will show that, while the wind forcing over the Nordic Seas has a strong impact on the circulation, changes in the Barents Sea's currents are mostly influenced by changes in sea ice cover and salinity, and that, eventually, changes in one region impact the other.

2) Data and methods

Altimeter data is obtained from CMEMS. The Sea Level Anomalies (SLA) are estimated using Optimal Interpolation on a regular latitude-longitude grid, with a resolution of 0.25°. It was

obtained by merging the L3 along-track measurements from both altimeter Copernicus missions, like Sentinel-6A and Sentinel-3A/B, and other collaborative missions including Jason-1, OSTM/Jason-2, Jason-3, Saral[-DP]/AltiKa, Cryosat-2, Topex/Poseidon, Envisat, GFO, ERS-1/2 and Haiyang-2A/B/C.

The Sea Surface Temperatures (SST) were extracted from the Multi Observation Global Ocean ARMOR3D L4 analysis. It consists of 3D fields of temperature, salinity, sea surface height, geostrophic currents and mixed layer depth, and available on a 0.25° regular grid.

A Sea Surface Salinity (SSS) and Sea Surface Density (SSD) product from CMEMS was also used. It was obtained through a multivariate optimal interpolation algorithm relying on Soil Moisture Ocean Salinity (SMOS) satellite images and in situ salinity measurements, combined with satellite SST information. The product was developed by the Consiglio Nazionale delle Ricerche (CNR).

Finally, datasets for the wind and the sea ice cover were extracted from the ERA5 reanalysis, the latest climate reanalysis produced by ECMWF, which provides data on many atmospheric, land-surface and sea-state parameters on a regular latitude-longitude grid with a resolution of 0.25°.

All datasets have monthly resolution and cover the time-period 1993-2020 (28 years).

To investigate the dominant mode of the circulation of the region, we performed a Principal Component Analysis (PCA) on the Sea Level Anomaly (SLA) - after removing the mean value for each month. The corresponding anomalies in the geostrophic currents were then calculated. The results were compared to the first Empirical Orthogonal Function (EOF) of the wind stress curl over the North of the Nordic Seas, over a region including the Lofoten Basin and the Greenland Gyre. The impacts of the geostrophic current anomalies on the SST and sea ice cover were quantified by the regression analysis of SST and sea ice cover data on the first PC of the SLA.

To analyze long-term changes in the circulation we calculated the trends in SLA, surface salinity, SST, surface density and sea ice cover over the region. In each case, the trends were built using a linear, normalized and time-increasing index to compute the regressions of the different quantities. The resulting maps were then compared to understand the processes responsible for the observed trends.

3) Interrannual variability of the geostrophic currents: causes, consequences and links between the Nordic and the Barents Seas

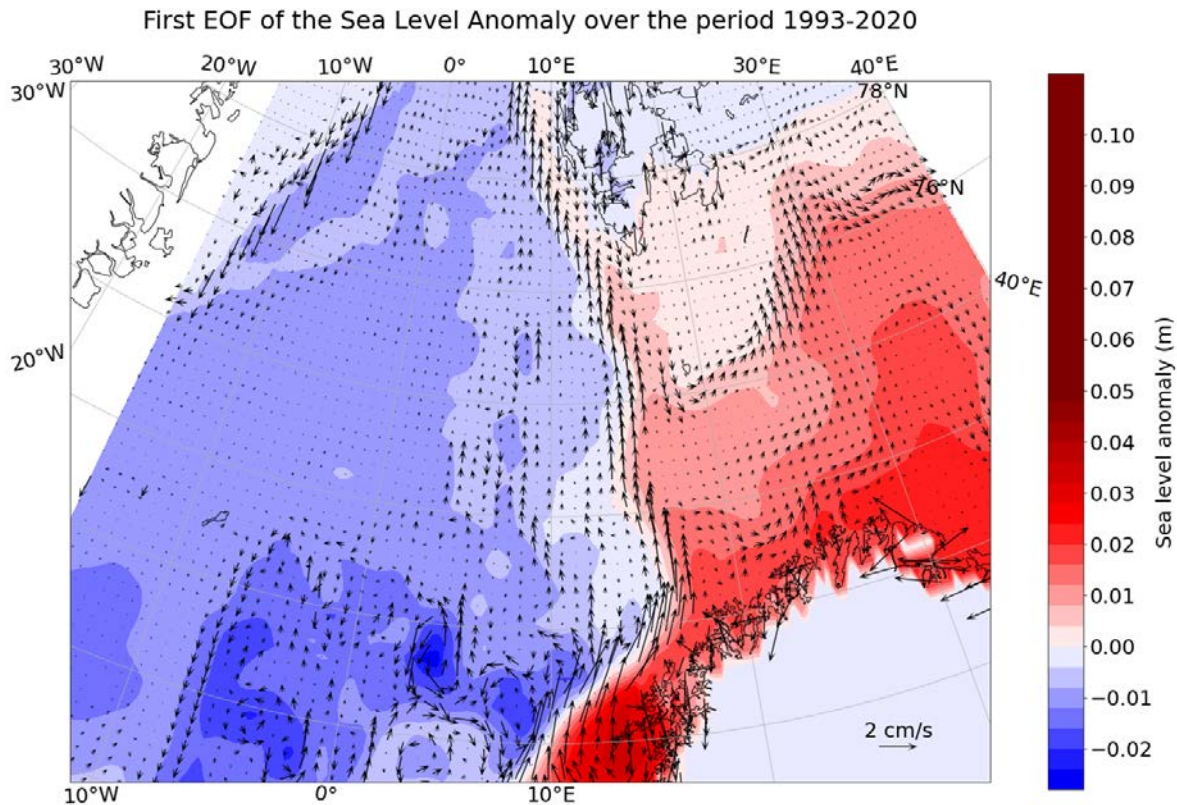   a) *Description of the main variability pattern*

Figure 38: First EOF of the Sea Level Anomaly (37% of the variability) between 1993 and 2020 – the corresponding geostrophic currents and geostrophic current anomalies are represented with small arrows

The first principle component of the SLA accounts for most of the variability (37% versus 11% for the second PC). It is characterized by a negative anomaly over the Lofoten Basin and the Greenland Sea and a positive anomaly above the Norwegian shelf and the Barents Sea (Figure 38). This translates into the strengthening of the eastern branch of the NwAC and of the WSC. An eastward anomalous current around Bear Island is also visible, which is representative of the weakening of the westward flowing mean current which brings cold waters into the Svalbard region. This anomaly is visible across all the Barents Sea, from 40°E to 15°E where it meets the WSC. This pattern thus implies changes in the water masses flowing through the WSC west of Svalbard, with an increase of the warm water input from the NwAC and a decrease in the colder water contribution coming from the Barents Sea.

Since all these currents are involved in important heat transports towards the Arctic region, the impact of the pattern described here on the SST are then analysed.

b) *Consequences on SST and sea ice*

The consequences of these circulation anomalies on the SST are a warming along the path of the northward currents all the way to the Fram Strait, the WSC and the recirculation branch (Figure 3b). The positive SST anomaly associated with the NwAC in the Nordic Seas can be linked to the strengthening of the NwAC via two processes: (1) an increase in transport of warm Atlantic Water along the NwAC, and/or (2) less heat loss in the stronger NwAC. It is well known that a faster and narrower ocean current loses less heat to the atmosphere in comparison to a weak and broader current (Furevik, 2001 [20]).

Further analysis shows that the long-term variability in the temperature anomaly in the Fram Strait is linked to the Sea level variability. Figure 39 (top), which shows the comparison of the temperature anomaly in the Fram Strait, calculated from the interpolated mooring data, and the

first principal component of SLA over both the Nordic and the Barents Seas, portrays the coherence between the long-term variability of the two time-series. A significant correlation (r = 0.50) is found between the two time series, after filtering them using a one-year filter. This correlation indicates that the temperature variability in the Fram Strait – and in particular the warm anomaly of 2006-07 – is linked to circulation anomalies on a much larger scale, at least over all of the Nordic Seas.

Such circulation anomalies do not only impact the heat transport to the Fram Strait, though. With a stronger current along the Norwegian shelf, a small increase of the volume transport through the BSO is also visible on SLA EOF1 (Figure 38) and could be associated with a general warming of the Barents Sea (Figure 39 - bottom). But mostly, the decrease of the westward current around Bear Island decreases the cold water input and clearly enhances the warming all along the anomalous current. The highest SST anomalies coincide perfectly with the eastward current anomalies (westward current slowing down). The weakening of the current could result in less cold waters transported from the Arctic region and hence induce the observed warming maximum.
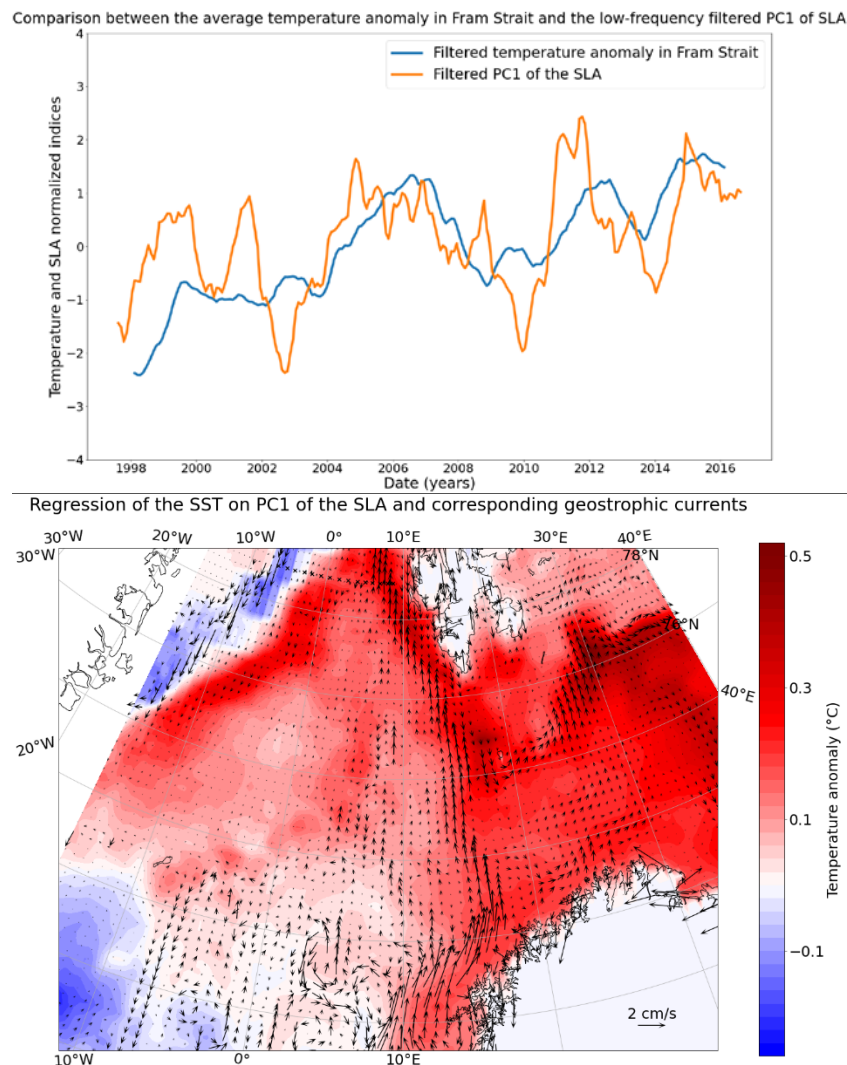

Figure 39: top: Comparison between the one-year-filtered average temperature in the Fram Strait calculated from the interpolation of mooring data and the one-year-filtered first principal component of the SLA – the correlation between the two time series is 0.50 – bottom: Regression of the SST on PC1 of the SLA, the corresponding geostrophic current

anomalies are represented with arrows. The black crosses show the locations of the AWI/NPI moorings.

Since the circulation pattern presented on Figure 38 is associated with a warming both in the Barents Sea and in the Fram Strait, an impact on sea ice melt can also be expected. Figure 40 confirms that a negative sea ice cover anomaly is correlated with high values of SLA PC1. This negative sea ice cover anomaly reaches local maxima along the westward current in the Barents Sea and the recirculation branch in the Fram Strait, where the SST was found to be strongly impacted.
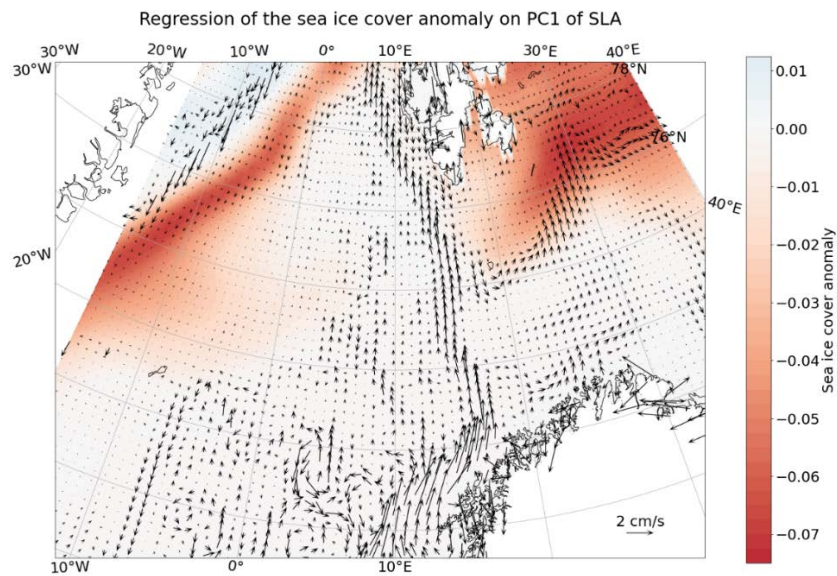

Figure 40: Regression of the sea ice cover anomaly on SLA PC1

c) *What is driving the variability of the current circulation?*

Next, we investigate the mechanisms associated with the changes in the SLA anomalies resulting in the circulation changes in the Nordic and Barents Sea. The large-scale atmospheric circulation is known to impact the sea level of the Nordic Seas (Chafik et al., 2017 [21]). Chatterjee et al. [14] already showed that atmospheric forcing could strengthen the Greenland Gyre and increase the warm water input to the Fram Strait. Here, we test a similar mechanism to explain the variability observed over a larger region, also including the Lofoten Basin and the Barents Sea.

We calculate the first PC of the wind curl over the northern Nordic Seas, excluding the Barents Sea. The first EOF shows a cyclonic anomaly over the whole region, and the regression of the SLA on the corresponding PC is very similar to the first EOF of the SLA (the two maps have a correlation of 0.98). The correlation between the first PC of the wind curl and the SLA is 0.45 which confirms the strong link between wind curl and SLA.
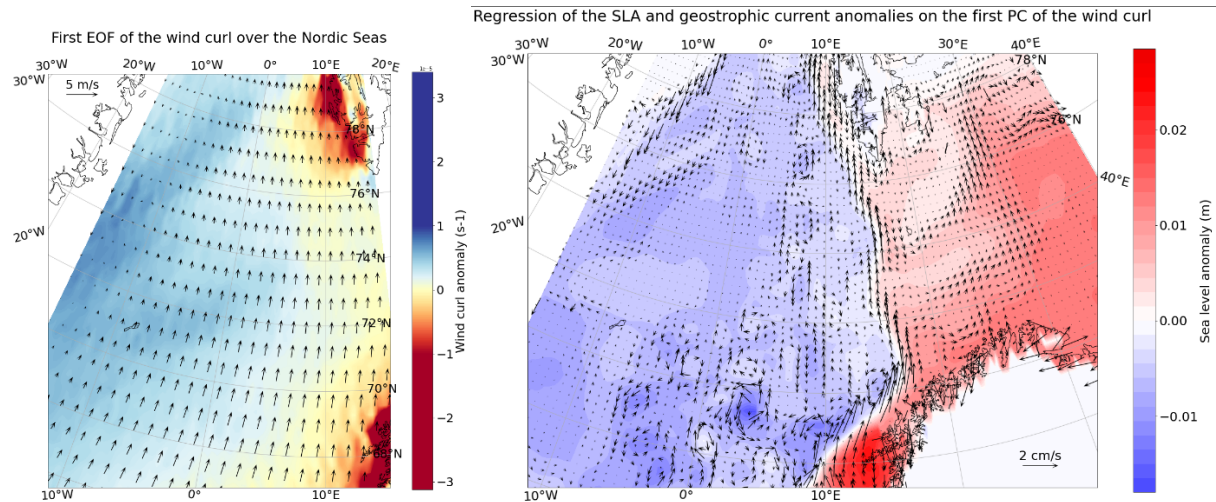
Figure 41: left: First EOF of the wind curl over the Nordic Seas (24% of the variability), the corresponding winds are represented with black arrows – right: Regression of the SLA on the first PC of the wind curl, the geostrophic currents anomalies are represented with black arrows.

A high correlation is also obtained if the Barents Sea is excluded from both PCA analyses of the SLA and the wind curl, which confirms the strong influence of the wind on the local circulation. But more interestingly, including the Barents Sea in both PCA analyses (wind curl and SLA) decreases the correlation with the first PC of the SLA (r=0.37) compared to when the wind curl PCA is only performed on the Nordic Seas. In particular, the previously anomalous eastward current in the Barents Sea is visible on Figure 41 (right), while the Barents Sea was excluded from the calculation of the wind curl PCs. This result suggests that the wind (and atmospheric pressure) anomalies over the Nordic Seas influence the oceanic currents locally, but could also have an indirect impact further east in the Barents Sea.

Another way to test this link between Nordic Seas winds and the Barents Sea is to consider its impact on sea ice cover, since we showed that sea ice cover was impacted by the circulation changes induced by SLA PC1.
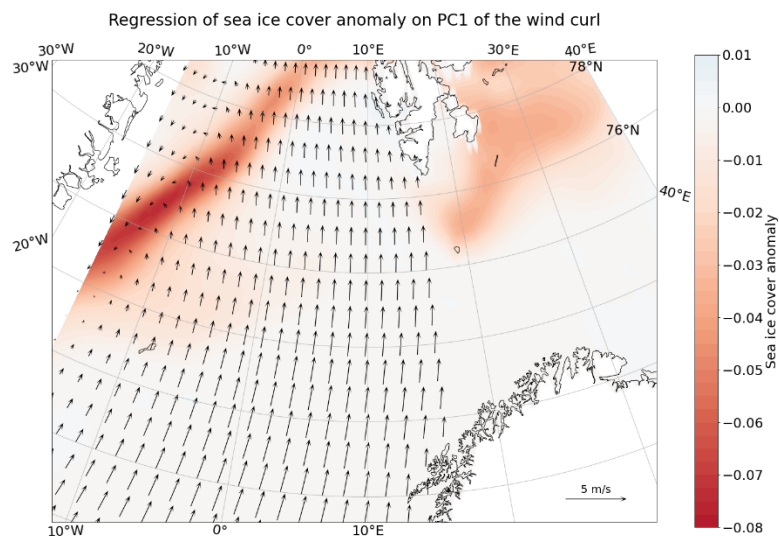

Figure 42: Regression of the sea ice cover anomaly over the first PC of the wind curl – the arrows indicate the corresponding wind anomalies over the region used in the PCA of the wind curl

Figure 42 shows that the months with a positive wind curl anomaly over the Nordics Seas had a negative sea ice cover anomaly over the Barents Sea (with correlations around -0.18 north east of Bear Island but significant at p = 0.01). Since PC1 of the wind curl does not show any positive trend, this correlation is not the effect of global warming, but is more likely the result of shorter-term variability. However, the nature of the link between wind and sea ice is not straightforward as several phenomena could be involved: southerly wind over the Barents Sea could warm the atmosphere and induce a melting from above, while a slow down of westward currents south of Svalbard (visible on Figure 39 - bottom) could warm the SST locally and induce a melting from below.

d) *Summary*

In this section, we showed that interannual circulation variability in the Nordic and Barents Sea was mostly driven by the wind curl over the Nordic Seas, which enhance the NwAC and its contribution to the WSC at the expense of the colder westward current coming from the Barents Sea. This circulation variability could be linked to both the temperature and sea ice cover variability in the Fram Strait and on a wider scale and provides a robust interpretation to the variability observed from the mooring data.

4) Trends in the circulation changes and surface water properties

a) *Different processes driving the circulation trends in the Nordic Seas and in the Barents Sea*

To understand the longer-term transformation of the oceanic circulation in the region, we now calculate the trend in deseasoned SLA and geostrophic currents as described previously. The mean value of the SLA over the region is removed for each month to hide the global sea level rise and focus on local circulation changes.
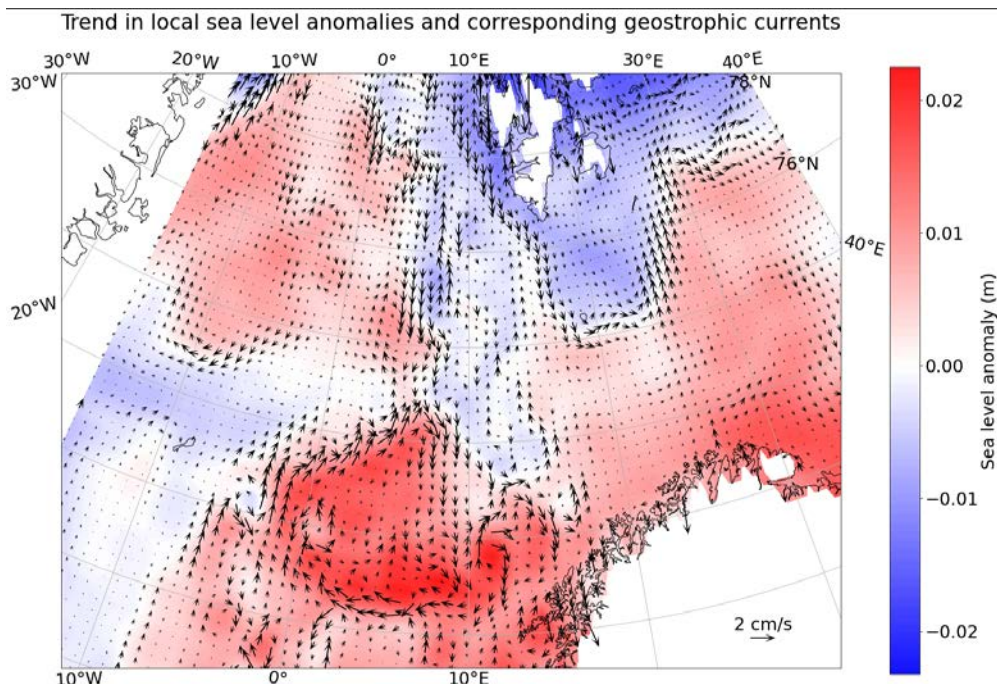

Figure 43: Trend in the local sea level anomalies between 1993 and 2020 and corresponding geostrophic current anomalies

In the Nordic Seas, the trend in SLA is characterized by a positive anomaly in the LB. The trend in the Barents Sea also shows a clear pattern, with a positive anomaly to the south and a negative anomaly to the north, inducing an eastward geostrophic current anomaly (weakening of the westward mean flow). We next demonstrate that these changes were mainly induced by changes in the salinity gradient between the north and the south of the Barents Sea.

Figure 44 presents the climatological means and trends in surface salinity during the time period 1993-2020. Both the mean and the trend show a good agreement between the salinity and density over the Barents Sea, which is not surprising since the salinity contribution to density tends to dominate over the temperature contribution in cold waters. In the warmer waters of the Nordic Seas, however, the contribution of temperature to density tends to take over and the correlation between salinity and density decreases. The mean state presented of Figure 44 is characterized by fresh and low-density waters along the coast of Norway and in ice-covered regions and more saline and dense waters in the LB, the Greenland Sea and in the southern Barents Sea. There, the trend has been an increasing freshening of the coastal waters to the south and an increase in salinity further north, modifying the surface density gradient subsequently.
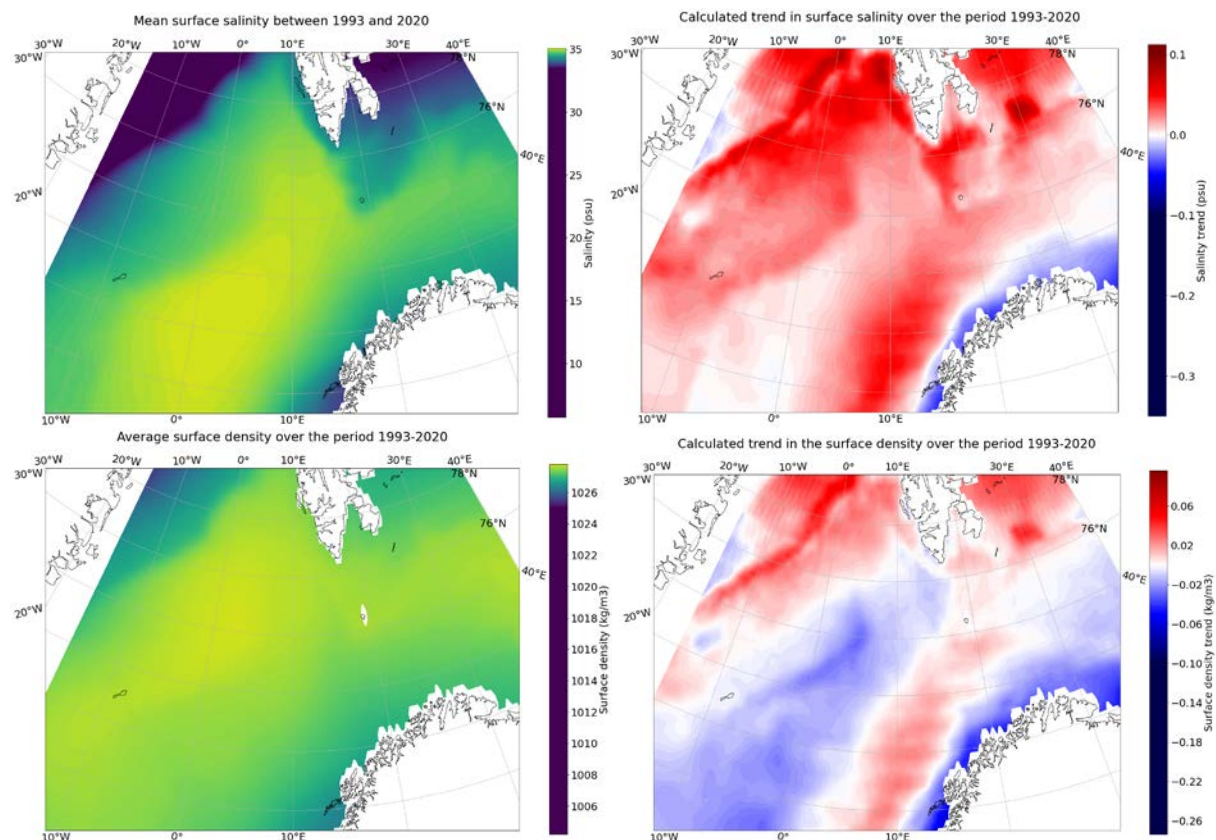
Figure 44: Mean surface salinity from satellite altimetry and trends in surface salinity between 1993 and 2020 (top) – Mean surface density and trends in surface density between 1993 and 2020 (bottom)

These changes in surface density have an impact on the steric part of the sea surface height but are not directly linked with the mass contribution to the SSH. Therefore, a link between density and SLA trends can be expected, but it is not straightforward either. The comparison between the trends in surface density and SLA is presented on Figure 45. Both trends compare very well in the Barents Sea where the steric part of the SSH thus seems to be dominant but show more differences in the Nordic Seas. More quantitatively, the correlation between surface density and SLA trends is only -0.30 when considering both the Nordic Seas and the Barents Sea, but it

drops to -0.75 when only the Barents Sea (east of 17°E) is considered. So, the SLA changes in the Nordic Seas and the Barents Sea respond to quite different mechanisms: in the Barents Sea, they mostly reflect changes in the steric height and density, themselves induced by salinity; and in the Nordic Seas, both the effect of temperature and the mass contribution to the SLA cannot be left aside.
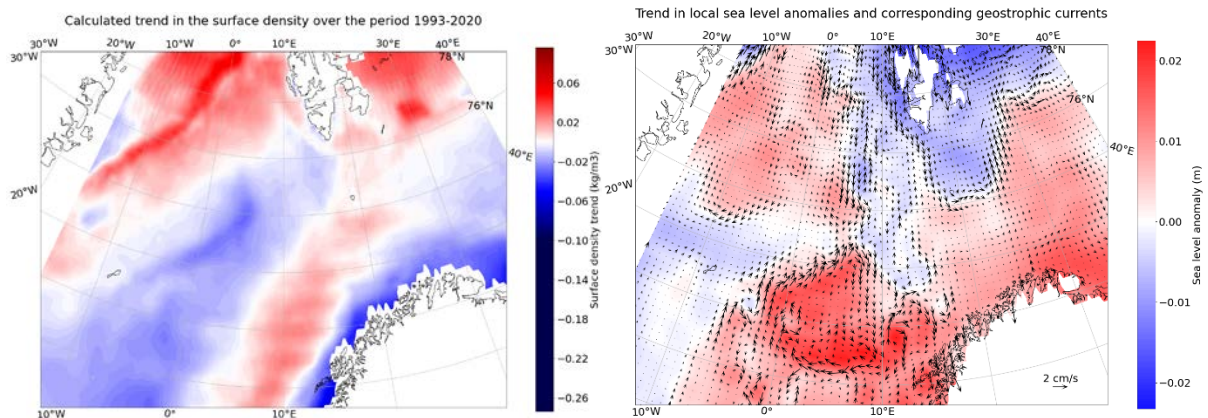

Figure 45: Comparison between the trends in surface density (left) and in sea level anomalies (right) – the correlation between the two is -0.30 for the whole region but drops to -0.75 when only the Barents Sea (east of 17°E) is considered.

This does not mean however that the mass contribution to the SLA trend in the Barents Sea is negligible. In particular, Heukamp et al. [22] tested another hypothesis to explain the decrease of the westward flow south of Svalbard: sea ice retreat and the subsequent local temperature anomaly could generate anomalous cyclonic winds over the region which would modify the SLA via Ekman transport anomalies.

b) *A feedback loop could enhance the warming south of Svalbard and in the WSC*

Being a region with one of the fastest sea ice decline, we can expect to find links between the trends in sea ice cover and surface salinity in the Barents Sea. The northern Barents Sea is a region where sea ice is normally imported from the Arctic [23]. Sea ice decline is expected to reduce this freshwater input and thus locally increase surface salinity. This result is consistent with Figures 44 and 46 which show the strongest decline in sea ice cover in the increasingly saline northern part of the Barents Sea.
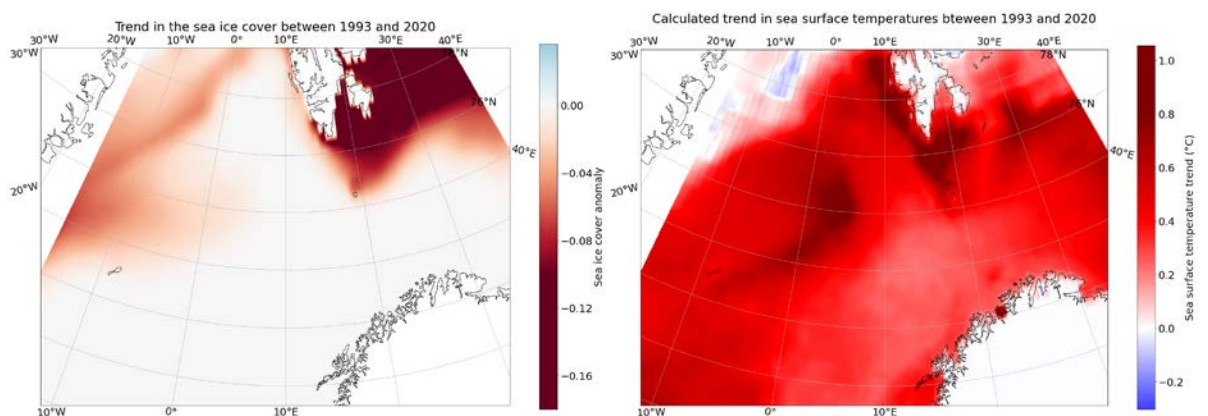

Figure 46: Trends in sea ice cover (left) and SST (right) during the time period 1993-2020 – the unit for sea ice cover is the average annual fraction of sea covered with ice.

Combining all the previous results, we propose a mechanism to explain the trends observed in the Barents Sea: the retreat of sea ice to the north limits the fresh input from meltwater and makes the surface waters more saline and denser, which creates a negative SLA anomaly to the north. This generates an eastward anomaly in the geostrophic currents in the Barents Sea, which translates into a decrease in the intensity of the westward current south of Svalbard.

What consequences can we expect from these changes? The water masses located east of Svalbard in the Barents Sea are relatively cold compared to the water masses located downstream as they mostly originate from ice-covered regions. A slow-down of this current can result in a decrease in the cold water transport and thus induce a warming downstream: south of Svalbard and in the WSC. The trend in the SST, presented on Figure 46, is consistent with this analysis: though a warming trend is visible everywhere, it is particularly important south and west of Svalbard. It should also be added that the trend in sea ice cover is not sufficient to interpret the warming pattern as a simple consequence of albedo changes, as the regions of maximum warming and maximum sea ice decline do not coincide with each other. Considering the oceanic circulation is thus necessary to account for the observed pattern: both a decrease in westward currents and a warming of upstream waters could enhance the SST increase west of Svalbard.

Besides, the eastward circulation anomaly in the Barents Sea also induces a local warming which could enhance the melting of sea ice around Svalbard and create a positive feedback loop. Though these results ought to be crosschecked with in situ observations in the Barents Sea to confirm that the velocity profiles follow the same trend as the geostrophic currents, the different trends show good consistency with each other.

c) *More complex interactions with salinity anomalies*

Our analysis shows that the Barents Sea mostly responds to local changes in the steric height, rather than to forcings by the local winds. If the role of the feedback loop described in the previous section was confirmed by in situ observations and models, the observed trends in the Barents Sea should continue for the next decade. However, though our analysis focused on trends calculated from a linear index, we should keep in mind that the evolution of water properties in the region over the past 25 years was anything but linear. In particular, several salinity anomalies were observed in the Nordic Seas and the Barents Sea over this period. First between 2005 and 2007, a high salinity anomaly was observed in all of the Nordic Seas and the Barents Sea as a consequence of stronger advection by the NwAC and the WSC. More recently, a low salinity anomaly was observed in the north Atlantic, following a change in the circulation of the subpolar gyre: instead of flowing south through the Labrador current, fresh waters were diverted eastwards across the Atlantic and towards the Nordic seas (Holliday et al., 2020 [24]). This freshwater anomaly is visible in the Nordic Seas in 2018-19, but also in the southern Barents Sea after advection through the BSO. The north of the Barents Sea however, mainly fed by currents from the east, remained mostly unaffected, which increased even more the local trend in the salinity gradient.

In fact, the main mechanisms driving the salinity anomaly are quite visible on the first two EOFs of the surface salinity over the Barents Sea, calculated over the region east of 12°E (25% and 16% of the variability).
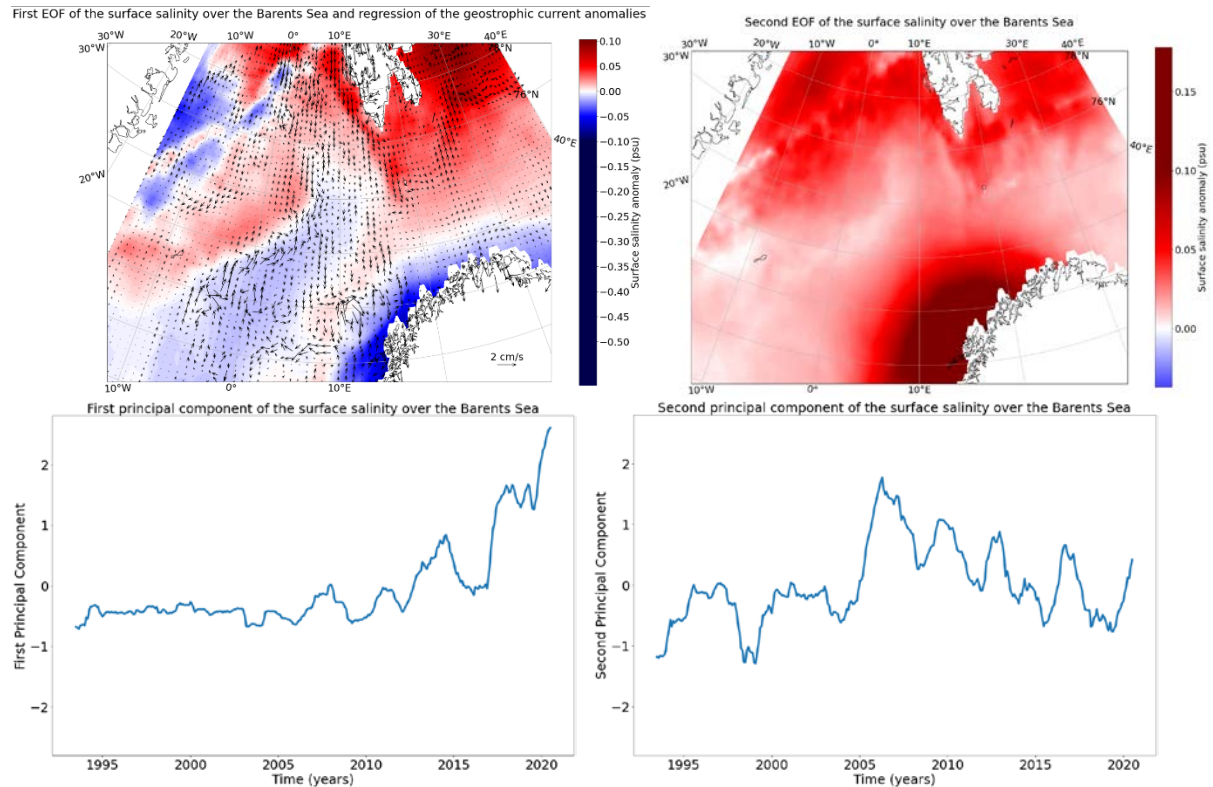
Figure 47: First EOF (25% of the variability, top left) of the surface salinity between 1993 and 2020 and regression of the geostrophic current anomalies - Corresponding time series (PC1, bottom left) – Second EOF (16% of the variability) and corresponding PC (PC2, right) – Calculation of the EOFs and PCs is done with the data east of 12°E even though the whole maps are shown. Both PCs are low-frequency-filtered with a 12-month moving average.

The first EOF reflects the impact of the decrease in sea ice cover with an increase in salinity well-correlated with the regions losing sea ice. The time series of the PC shows a non-linear increasing trend which accelerated after 2012. The regression of the geostrophic currents on this time series are superimposed on the EOF and confirm the results previously obtained using a linear trend. The second EOF shows a positive (or negative) salinity anomaly over the whole region. The time series of the PC shows a maximum between 2005 and 2007 corresponding to the already-mentioned anomalous advection of Atlantic Waters through the Nordic Seas. A local minimum is also visible in 2018-19 when the more recent freshwater anomaly was advected to the Nordic Seas. This complementary study highlights the complexity and the irregularity of the oceanic changes in the region, but also provides consistent results with the "linear trend approach".

d) *Consistent results with the mooring data and TOPAZ-4b*

The availability of the interpolated mooring data can once more be used to check the consistency between the trends and processes described in this section and the visible consequences in the Fram Strait. With a weakening of the westward current south of Svalbard, the meridional transport in the WSC is expected to show a decreasing trend.
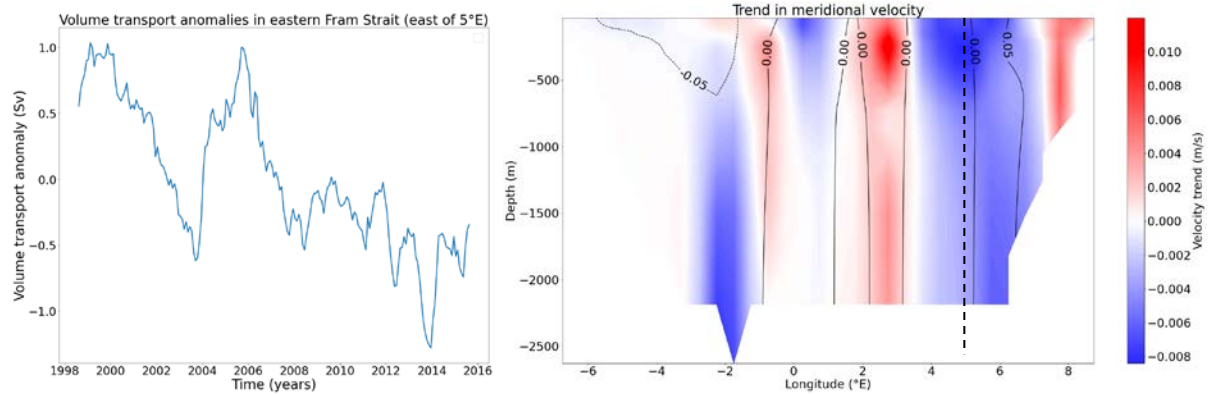
Figure 48: Two-year filtered meridional volume transport anomaly west of 5°E calculated from the interpolated mooring data (left) – Spatial trends in meridional velocities (right). The trend is built using a linear, normalized, time-increasing index. The contours show the mean meridional velocities.

The volume transport from the filtered mooring data shows a relatively significant decreasing trend east of 5°E (at p = 0.15 when considering the unfiltered time series). This trend is mostly caused by a weakening of the offshore branch of the WSC, west of 7°E. In 2012, Beszczynska-Möller et al. already observed such a trend [9], but the result was considered to be insignificant. The difference comes from the extension of the time series: when only considering the data before 2012 as was done in [9], we obtain a much lower significance.

Nevertheless, choices made during the interpolation may also have an impact. Contrary to the interpolated temperature products, the velocity interpolations did not reconstruct the current anomalies when data was missing, and the uncertainty on parts of the time series with missing data, in particular 2013-2016, could be as high as 1Sv.

So the results from the mooring interpolation are consistent with the trend obtained with altimeter data, but with a low significance. The question of the precise location in the Fram Strait of the water masses coming from the Barents Sea is also still open: showing that they are part of the offshore branch would provide a useful confirmation of the previous results.

Though TOPAZ-4b was shown in the previous chapter to simplify the current structure in the Fram Strait, it could capture interannual variability and the trends related to global warming. Here we use it to visualize and check the decreasing intensity of the current south of Svalbard due to the poor coverage of the region by measurement campaigns. We show on Figure 49 the results for a meridional section at 18°E, between 72°N and 77°N. The trends are defined with the same index that was used for observation data.
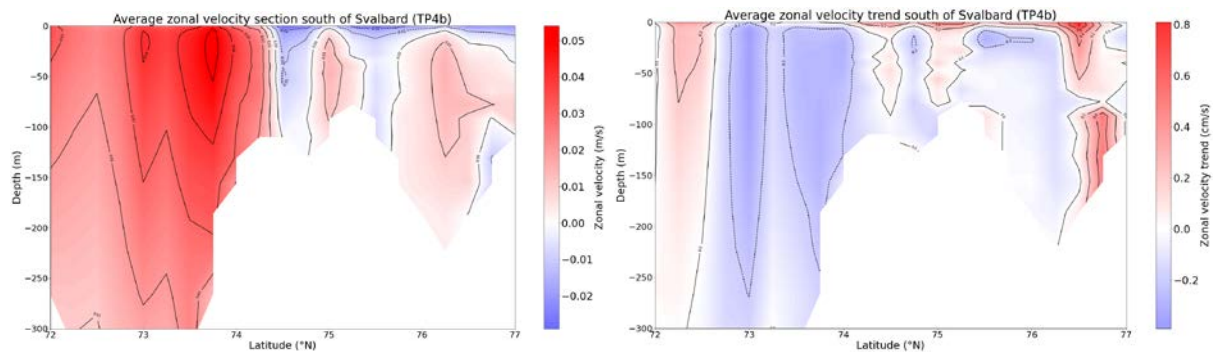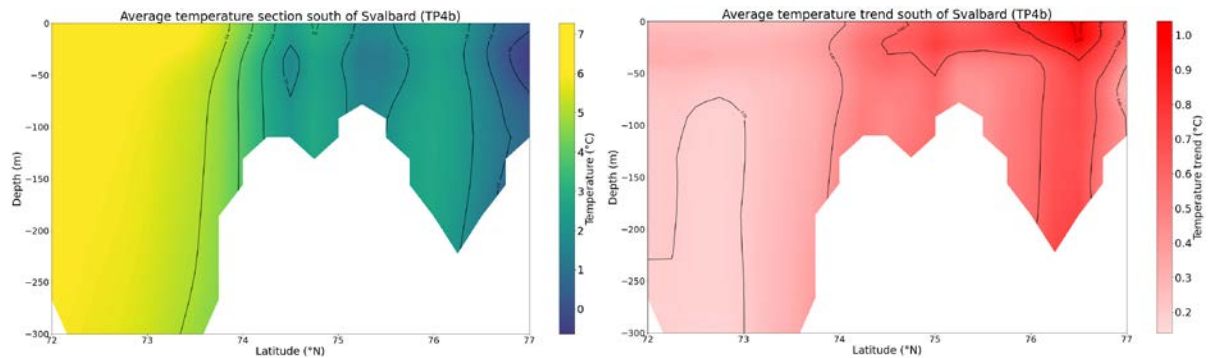
Figure 49: Average zonal velocity and temperature sections in the Barents Sea at 18°E (left) from TOPAZ-4b. The zonal velocity is considered to be positive when oriented eastwards. – Trends in zonal velocity and temperature between 1993 and 2020 (right) from TOPAZ-4b.

TOPAZ-4b confirms the existence of a westward flow south of Svalbard, between 74 °N and 77°N. This flow is confined at the surface, in the first 50m of the ocean, and transports cold waters (less than 2°C) towards the WSC. The trend in TOPAZ-4b is a significant weakening of this flow over the study period, with velocity trends as high as 20 to 30% of the average velocity. The temperature trend shows that the parts of the section with the fastest warming are well correlated spatially with this decreasing westward flow, which is consistent with a decrease of cold water advection.

5) Summary and discussion

a) *Different processes impact the circulation in the Nordic Seas and in the Barents Sea*

The Nordic Seas and the Barents Sea were found to be affected by distinct forcings. While the wind is the main driver for circulation anomalies – and temperature anomalies due to advection – in the first case, the Barents Sea circulation was mostly affected by changes in sea ice and water properties. We propose here one explanation for these differences.
We mentioned earlier that the main geostrophic currents at high latitudes were following the bathymetry. This means that, under the influence of a wind curl, the circulation will only spin up if the bathymetry allows it. Even in the very simple gyre models developed by Sverdrup in 1947, the presence of boundaries east and west of the ocean are necessary to the formation of the gyre. In the Nordic Seas, both the Greenland Sea and the Lofoten Basin are deep basins with clear bathymetric boundaries in all directions. Cyclonic gyres are present and can therefore respond to an anomalous wind curl, provided that it has a similar geographical extent. In the Barents Sea, the situation is quite different with a shallower bathymetry and no west boundary closing the basin. The main currents there still tend to follow bathymetric features such as the Norwegian shelf or the northern boundary of Bear Island trough. Yet no closed basin allows to convert wind curl anomalies in geostrophic currents.

b) *Interactions between the two regions*

Though the circulations in the Nordic Seas and the Barents Sea are governed by distinct mechanisms, the subsequent circulation changes have consequences beyond the boundaries of each basin. Wind-induced circulation changes in the Nordic Seas impact the currents and the sea ice cover in the Barents Sea, and salinity-induced changes in the Barents Sea are eventually advected to the WSC. Thus, the regression of the SLA on PC1 of the wind curl over the Nordic Seas was also very similar to the first EOF of the SLA over the Barents Sea. Similarly, the trends observed south and west of Svalbard showed a good geographical continuity, suggesting

that changes in the Northern Barents Sea were advected to the WSC. In each case, a decrease in the intensity of the westward current south of Svalbard seemed to be involved. Whether an indirect consequence of changes in the winds and currents further west or in the local salinity gradient, such a weaker current was associated with a continuous warm anomaly in the northern Barents Sea and the WSC, confirming the strong links in the trends and variability of both regions.

Conclusion

This report on the oceanography of the Fram Strait was structured around the interpolation of the data from the AWI/NPI moorings between 1997 and 2016. We first presented a method to interpolate the temperatures with a monthly and a daily resolution and adapted it to salinity and current velocities. The availability of these new interpolation products allowed us to understand the links between pointwise and integral measurements using the acoustic data from the ACOBAR project. It was also used to evaluate the coupled ocean-sea ice model TOPAZ-4b in the Fram Strait region and suggest ideas to improve the reliability of the model.

With a larger number of data products for the Fram Strait and the Nordic Seas, whose consistency and limits have been studied, it becomes possible to push further our understanding of the physical mechanisms driving the variability in the region. This was done in the fourth chapter of this report, in which we showed the differences between the forcings impacting the Nordic Seas and the Barents Sea, but also the reciprocal interactions between them. We highlighted that the interannual variability observed in the Fram Strait mooring temperatures was largely influenced by large scale circulation variability ruled by the atmospheric forcing over the Nordic Seas. The enhanced ocean warming trend west of Svalbard, on the other hand, could be the consequence of very distinct processes, most likely linked to the fast sea ice decline in the Barents Sea. Both observation and model data show a decrease in the westward flow south of Svalbard, which normally brings cold water to the WSC. More generally, the fourth chapter of this report suggests than ocean changes in circulation, temperature, salinity and even sea ice in the Nordic Seas, Fram Strait and the Barents Sea mostly follow two common variability modes: on the interannual time scale, cyclonic winds determine the relative importance of the contribution of AW in the region via enhanced or weakened AW transport ; and on longer-time scales, Atlantification and sea ice loss of the Barents Sea decreases the contribution of Arctic Waters locally and further west in Fram Strait.

Pushing further the analysis of the trends in the Fram Strait would require better estimates of the meridional currents. Progress will be made with the next inputs from the mooring line and high-resolution models will certainly have a role to play. The general question will be to know whether fast changes in the region will eventually modify the circulation driving the heat transport to the Arctic, either due to a decreased input from the Barents Sea to the WSC or to changes in the EGC, which is mostly driven by the thermal wind and should be impacted by the temperature and salinity changes in the strait. Ultimately, the consequences on sea ice decline in the Arctic or on the AMOC via deep water formation in the Greenland and Barents Sea should be addressed, as they are responsible for the strong links between the local oceanography and the global climate.

References

[1] Overland, J*., Hanna, E*., Hanssen-Bauer, I*., Kim, S.-J*., Walsh, J*., Wang, M*., & Bhatt, U. *(2019).* [The Arctic] surface air temperature [in "State of the Climate in 2018"]. Bulletin of the American Meteorological Society*, 100(9),* S142–S144.

[2] Screen, J. A. & Simmonds, I. Increasing fall-winter energy loss from the Arctic Ocean and its role in Arctic temperature amplification. *Geophys. Res. Lett.* **37**, L16707 (2010).

[3] Broomé, S., Chafik, L., & Nilsson, J. (2021). A satellite-based Lagrangian perspective on Atlantic Water fractionation between Arctic gateways. Journal of Geophysical Research: Oceans, 126, e2021JC017248. https:// doi.org/10.1029/2021JC017248

[4] Hattermann, T., P. E. Isachsen, W.-J. von Appen, J. Albretsen, and A. Sundfjord (2016), Eddy-driven recirculation of Atlantic Water in Fram Strait, Geophys. Res. Lett., 43, 3406–3414, doi:10.1002/ 2016GL068323.

[5] Johannessen, O.M. (1986). Brief Overview of the Physical Oceanography. In: Hurdle, B.G. (eds) The Nordic Seas. Springer, New York, NY. https://doi.org/10.1007/978-1-4615-8035-5_4

[6] Swift, J.H. (1986). The Arctic Waters. In: Hurdle, B.G. (eds) The Nordic Seas. Springer, New York, NY. https://doi.org/10.1007/978-1-4615-8035-5_5

[7] Knut Aagaard, L.K. Coachman, Eddy Carmack, On the halocline of the Arctic Ocean, Deep Sea Research Part A. Oceanographic Research Papers, Volume 28, Issue 6, 1981, Pages 529-545, ISSN 0198-0149, https://doi.org/10.1016/0198-0149(81)90115-1.

[8] Von Appen, W.-J., U. Schauer, T. Hattermann, and A. Beszczynska-Möller (2016), Seasonal cycle of mesoscale instability of the West Spitsbergen Current, J. Phys. Oceanogr., doi:10.1175/JPO-D-15-0184.1, in press

[9] Beszczynska-Möller, A., Fahrbach, E., Schauer, U., and Hansen, E. 2012. Variability in Atlantic water temperature and transport at the entrance to the Arctic Ocean, 1997–2010. – ICES Journal of Marine Science, 69: 852–863.

[10] H. Sagen, P.F. Worcester, M.A. Dzieciuch, F. Geyer, S. Sandven, M. Babiker, A. Beszczynska-Möller, B.D. Dushaw, B. Cornuelle, Resolution, identification, and stability of broadband acoustic arrivals in Fram Strait, J. Acoust. Soc. Am. 141 (2017) 2055–2068, doi:10.1121/1.4978780

[11] F. Geyer, H. Sagen and B. Dushaw et al. A dataset consisting of a two-year long temperature and sound speed time series from acoustic tomography in Fram Strait. Data in Brief 42 (2022) 108118

[12] P. Sakov, F. Counillon, L. Bertino, K. A. Lisæter, P. R. Oke, and A. Korablev (2012). TOPAZ4: an ocean-sea ice data assimilation system for the North Atlantic and Arctic. Ocean Sci., 8, 633–656, 2012. www.ocean-sci.net/8/633/2012/

[13] Jiping Xie, Laurent Bertino, François Counillon, Knut A. Lisæter, and Pavel Sakov (2016). Quality assessment of the TOPAZ4 reanalysis in the Arctic over the period 1991–2013. Ocean Sci., 13, 123–144, 2017. www.ocean-sci.net/13/123/2017/

[14] Chatterjee, S., Raj, R. P., Bertino, L., Skagseth, Ø., Ravichandran, M., & Johannessen, O. M. (2018). Role of Greenland Sea gyre circulation on Atlantic Water temperature variability in the Fram Strait. Geophysical Research Letters, 45. https://doi.org/10.1029/2018GL079174

[15] Wang, Q., Wekerle, C., Wang, X., Danilov, S., Koldunov, N., Sein, D., et al. (2020). Intensification of the Atlantic Water supply to the Arctic Ocean through Fram Strait induced by Arctic sea ice decline. Geophysical Research Letters, 47, e2019GL086682. https://doi.org/10.1029/2019GL086682

[16] Takamasa Tsubouchi Wilken-Jon von AppenUrsula Schauer, 2017. Observed Arctic Ocean volume and heat transports during 2004-2010. Arctic sea ice WS @ Bergen.

[17] S. A. Dyer and J. S. Dyer, "Cubic-spline interpolation. 1," in *IEEE Instrumentation & Measurement Magazine*, vol. 4, no. 1, pp. 44-46, March 2001, doi: 10.1109/5289.911175.

[18] Hans Wackernagel, Linear Geostatistics – Lecture Notes. Chapter 10: Ordinary kriging. Master STEPIPGP - Université Paris Diderot, Equipe de Géostatistique, Centre de Géosciences, MINES ParisTech, 2011. http://hans.wackernagel.free.fr

[19] Wekerle, C., Wang, Q., von Appen, W.-J., Danilov, S., Schourup-Kristensen, V., & Jung, T. (2017). Eddy-resolving simulation of the Atlantic Water circulation in the Fram Strait with focus on the seasonal cycle. Journal of Geophysical Research: Oceans, 122, 8385–8405. https://doi.org/10.1002/ 2017JC012974

[20] T. Furevik, Annual and interannual variability of Atlantic Water temperatures in the Norwegian and Barents Seas: 1980–1996, Deep-Sea Research Part I 48 (2001) 383-404

[21] Chafik, Léon & Nilsen, Jan Even & Dangendorf, Sönke. (2017). Impact of North Atlantic Teleconnection Patterns on Northern European Sea Level. Journal of Marine Science and Engineering. 5. 10.3390/jmse5030043.

[22] Heukamp, F. and Kanzow, T.: Investigations on the coupling of the Barents Sea sea-ice retreat on the Atlantic Water inflow via an ocean-ice-wind feedback in the context of Arctic Amplification , EGU General Assembly 2022, Vienna, Austria, 23–27 May 2022, EGU22-10191, https://doi.org/10.5194/egusphere-egu22-10191, 2022.

[23] Kwok, R., 2009: Outflow of Arctic Ocean sea ice into the Greenland and Barents Seas: 1979–2007. J. Climate, 22, 2438–2457, https://doi.org/10.1175/2008JCLI2819.1.

[24] Holliday, N. P., Bersch, M., Berx, B., Chafik, L., Cunningham, S., Florindo-lópez, C., Hátún, H., Johns, W., Josey, S. A., Larsen, K. M. H., Mulet, S., Oltmanns, M., Reverdin, G., Rossby, T., Thierry, V., Valdimarsson, H., & Yashayaev, I. (2020). Ocean circulation causes the largest freshening event for 120 years in eastern subpolar North Atlantic. *Nature Communications*, *11*(1). https://doi.org/10.1038/s41467-020-14474-y

[25] Barton, B. I., Lenn, Y.-D., Lique, C. (2018). Observed Atlantification of the Barents Sea causes the polar front to limit the expansion of winter sea ice. Journal of Physical Oceanography, Volume 48 184ç-1866. https://doi.org/10.1175/JPO-D-18-0003.1